

Durham E-Theses

MT-MOT: a Hybrid Magnetic Trap / Magneto-Optical Trap

WALKER, PAUL,ARBUTHNOT

How to cite:

WALKER, PAUL,ARBUTHNOT (2018) *MT-MOT: a Hybrid Magnetic Trap / Magneto-Optical Trap*, Durham theses, Durham University. Available at Durham E-Theses Online:
<http://etheses.dur.ac.uk/12941/>

Use policy

The full-text may be used and/or reproduced, and given to third parties in any format or medium, without prior permission or charge, for personal research or study, educational, or not-for-profit purposes provided that:

- a full bibliographic reference is made to the original source
- a [link](#) is made to the metadata record in Durham E-Theses
- the full-text is not changed in any way

The full-text must not be sold in any format or medium without the formal permission of the copyright holders.

Please consult the [full Durham E-Theses policy](#) for further details.

MT-MOT: a Hybrid Magnetic Trap / Magneto-Optical Trap.

Paul Arbuthnot Walker

A thesis submitted in fulfilment
of the requirements for the degree of
Master of Science by Research



Department of Physics

Durham University

February 2018

Abstract

Arrays of cold atoms in magnetic traps have been implemented for use in quantum simulation, metrology, and ultracold chemistry. The scope of all of these fields could be greatly enhanced with cold and ultracold molecules. Cooling and trapping molecules, however, poses unique challenges compared to atoms. Sympathetic cooling, whereby molecules are cooled via collisions with ultracold atoms, will be a key technique for achieving the required densities and temperatures.

Towards this end, the Carty group in Durham has constructed a moving-trap Zeeman decelerator ('MTZD'), based on the same operating principles as a conventional Zeeman decelerator but producing a truly dynamic three-dimensional trapping potential. We have begun to characterise the decelerator with metastable argon, showing 3D guiding and deceleration, and intend to move to molecules in the near future.

In the longer term the decelerator is intended to load a magnetic trap. Presented here are the findings from preliminary work to design a hybrid magnetic trap with magneto-optical trap capability, or 'MT-MOT'. The MT-MOT comprises six toroidal permanent magnets plus switchable electromagnetic coils. We have performed simulations to determine the feasibility of co-loading lithium atoms and calcium hydride molecules. Some consideration of loss mechanisms and likely trap lifetimes are discussed.

Declaration

The work in this thesis is based on research carried out at the Department of Physics, the University of Durham, United Kingdom, between October 2016 and September 2017.

It is all my own work unless referenced to the contrary in the text. I confirm that no part of the material offered has previously been submitted by myself for a degree in this or any other University.

Paul A. Walker

Durham, February, 2018

The copyright of this thesis rests with the author. No quotation from it should be published without their prior written consent and information derived from it should be acknowledged.

For Jim Goodwin, and Mr Tompkins.

Acknowledgements

I would like to express my gratitude to my supervisor, Dr. David Carty, for taking a chance and offering me the opportunity to work on this interesting project. I am also grateful to my predecessors Dr. Lewis McArd and Dr. Arin Mizouri for entrusting me with their baby (not that they had much choice). As my immediate predecessor Lewis in particular was always willing to explain the arcana of the decelerator to me, and on the few times I have worked with Arin her advice on the vacuum system and detector was invaluable.

I could also not have got through this year without the endless supply of reasonably-priced caffeine provided by Lynn and Catherine in the Bransden room, and similarly I must acknowledge the fine selection of ale (and pies) in the Station House, (to say nothing of the free wireless).

I would like to thank the reprobates in Rooster's Cat, Durham Rams, and Benfieldside, for giving me something to do that involved no physics whatsoever, and arguably keeping me sane(!)

Mijn lieve Martina, bedankt voor jouw geduld, en ook bedankt dat je me in de frisse lucht hebt laten lopen. Het zal erger worden voordat het beter wordt!

Contents

| | | |
|----------|---|-----------|
| 1 | Introduction | 1 |
| 1.1 | Why ultracold molecules? | 1 |
| 1.2 | How ultracold molecules? | 2 |
| 2 | Theory and background | 3 |
| 2.1 | The Zeeman effect | 3 |
| 2.2 | Laser cooling | 7 |
| 2.3 | Magnetic confinement | 7 |
| 2.4 | The Durham decelerator | 9 |
| 2.5 | Magneto-optical traps | 10 |
| 2.6 | Beyond laser cooling | 12 |
| 3 | Magnetic trap design | 13 |
| 3.1 | Trap components | 13 |
| 3.2 | Trap depth | 14 |
| 3.3 | Trap fields | 16 |
| 4 | Simulation methodology | 19 |
| 4.1 | Field interpolation - spline | 19 |
| 4.2 | Field interpolation - tricubic | 20 |
| 4.3 | Numerical methods - Runge-Kutta | 23 |
| 4.4 | Numerical methods - velocity Verlet | 25 |
| 4.5 | Numerical integrator errors | 28 |
| 5 | Results | 31 |
| 5.1 | Trap loading - 1D simulation | 31 |
| 5.2 | Trap loading - 3D simulation | 32 |

| | | |
|----------|---|-----------|
| 5.3 | Trap loading - slower coil current | 34 |
| 5.4 | Trap loading - coil switching times | 36 |
| 5.5 | Trap acceptance | 39 |
| 5.6 | Trap losses | 40 |
| 5.7 | Majorana losses | 42 |
| 5.8 | Trap cooling - atomic density | 45 |
| 5.9 | Trap cooling - laser interaction | 46 |
| 6 | Conclusions | 47 |
| 6.1 | Review | 47 |
| 6.2 | Outlook | 48 |

Chapter 1

Introduction

We propose a hybrid magnetic trap / magneto-optical trap (MT-MOT) which would be loaded with co-decelerated calcium hydride (CaH) molecules and lithium (Li) atoms from our moving-trap Zeeman decelerator (MTZD). This chapter discusses our motivation and states our proposed methodology.

1.1 Why ultracold molecules?

The MTZD was built as part of the MicroKelvin Molecules in a Quantum Array (MMQA) programme grant, which focused on achieving quantum simulation with low-temperature molecules. The term ‘ultracold’ is used to mean temperatures less than 1 mK. Low-density vapours of ultracold atoms are used in condensed-matter studies as analogues of other systems [3], such as interesting liquid phases, or electrons in a solid. The atoms are typically confined in an optical lattice with parameters that are easy to characterise and tune, allowing the interatomic interactions to be controlled. As an example [4]; electrons in a conductor move with typical velocities of order 10^6 m s^{-1} through an atomic lattice with node separations on the order of 10^{-9} m , giving a timescale for these interactions of order 10^{-15} s . In contrast, atoms in a quantum simulator move with typical velocities of 10^{-3} m s^{-1} between wells that are perhaps 10^{-7} m apart, meaning a timescale of order 10^{-3} s . This makes direct, real-time imaging feasible for analogues of otherwise inaccessible phenomena. Although the nature of a simulator can be adjusted through the choice of atomic species and the applied laser fields, there are limitations to the systems that can be explored. A promising approach is the use of polar molecules, which have strong, long-range dipole interactions and a rich internal energy structure.

Experiments studying the reaction rates of chemical processes have shown the dependence of these rates on the hyperfine state or magnetic sublevel of one or more of the reactants - see for example the production of KRb by Ospelkaus *et al.* [5]. This paves the way for possible control or suppression of chemical reactions. Ultralow temperature reactions could

also illuminate the effects of long-range, weak intermolecular forces on reaction dynamics [6].

1.2 How ultracold molecules?

Setting up a sample of ultracold molecules rather than atoms is, however, easier said than done. In some cases this can be achieved by cooling atoms and then associating them to produce cold molecules, using photoassociation [5, 7] or Feshbach / magnetoassociation [8]. These techniques have been very successful, but rely on reactants that can be laser-cooled.

Atomic traps are often loaded by a Zeeman slower [9]. Both of these technologies, however, rely on laser cooling [10], which does not work for most molecules - the same complex internal energy structure that makes them attractive for experimental purposes works against the experimentalist, by removing the necessary closed optical cycles. Some groups have demonstrated laser cooling and slowing of diatomic molecules such as CaF [11], and even achieved a magneto-optical trap with SrF [12], but these are exceptional cases. To work with a broader range of molecular species requires a different approach.

Various techniques to decelerate and trap paramagnetic neutral species using electromagnetic interactions have been demonstrated, including Stark, Rydberg-Stark or Zeeman deceleration [13]. A Zeeman decelerator [14, 15] uses time-varying magnetic fields to manipulate radicals; Akerman *et al.* [16] have recently decelerated a dual-species beam of O₂ and Li using this technique. We propose to Zeeman decelerate a laser ablation-produced buffer-gas beam of CaH molecules and Li atoms with a post-deceleration internal temperature of 45 mK. We expect to be able to produce a beam containing 5×10^{10} CaH molecules per steradian [17], with the Li being up to 10^4 times brighter [18]. We have demonstrated deceleration of metastable Ar(³P₂) from 360 m s^{-1} to 270 m s^{-1} [2], and extending our current decelerator would allow us to decelerate the CaH / Li sample from 150 m s^{-1} to 11 m s^{-1} . This sample would then be loaded into a hybrid magnetic trap / magneto-optical trap to laser-cool the Li, which would then sympathetically cool the CaH. Chapter 2 gives the theoretical background for this, including the progress we have made so far.

Chapter 2

Theory and background

2.1 The Zeeman effect

A magnetic dipole (with moment $\boldsymbol{\mu}$) in a magnetic field (\mathbf{B}) experiences a torque, giving rise to potential energy:

$$U = -\boldsymbol{\mu} \cdot \mathbf{B}. \quad (2.1.1)$$

Paramagnetic atoms or molecules have a magnetic dipole moment, due to possessing an unpaired electron. Classically, a current loop produces a magnetic moment, and the angular momentum of the orbiting electron is analogous to this. Nuclear spin can also produce a magnetic moment, but we shall initially consider an atom with zero nuclear spin. The electron moment has two components - firstly, the orbital moment $\boldsymbol{\mu}_L$, due to the orbital angular momentum \mathbf{L} , given in terms of the elementary charge e and the electron mass m_e :

$$\begin{aligned} \boldsymbol{\mu}_L &= g_L \frac{-e}{2m_e} \mathbf{L} \\ &= -g_L \mu_B \frac{\mathbf{L}}{\hbar}, \end{aligned} \quad (2.1.2)$$

where g_L is the g-factor for orbital angular momentum of an electron, and μ_B is the Bohr magneton, defined as:

$$\mu_B = \frac{e\hbar}{2m_e}. \quad (2.1.3)$$

The second component arises from the electron spin. Noting that the g-factor g_S is not the same as in the orbital case, spin moment $\boldsymbol{\mu}_S$ is related to the spin angular momentum \mathbf{S} :

$$\begin{aligned} \boldsymbol{\mu}_S &= g_S \frac{-e}{2m_e} \mathbf{S} \\ &= -g_S \mu_B \frac{\mathbf{S}}{\hbar}. \end{aligned} \quad (2.1.4)$$

Due to their interaction, the orbital and spin angular momenta couple and are not independently conserved, so the total angular momentum $\mathbf{J} \equiv \mathbf{L} + \mathbf{S}$ is the appropriate attribute

to deal with. For \mathbf{J} the Landé factor g_J combines the orbital and spin contributions. This gives:

$$\begin{aligned}\boldsymbol{\mu}_J &= g_J \frac{-e}{2m_e} \mathbf{J} \\ &= -g_J \mu_B \frac{\mathbf{J}}{\hbar}.\end{aligned}\tag{2.1.5}$$

The component of \mathbf{J} projected along the direction of \mathbf{B} is quantised - if \mathbf{B} is in the z -direction, we get $J_z = m_j \hbar$, where m_j is the total angular momentum projection quantum number. Combining the expressions for potential energy and magnetic moment gives the Zeeman shift in the energy level of the particle:

$$\Delta E = g_J \mu_B m_j B.\tag{2.1.6}$$

This means that for a given field strength B , the allowed values of m_j give a series of equally spaced shifts in the energy level of the atom or molecule, both above and below the ground state. Our Zeeman decelerator experiment currently uses argon excited to a 3P state. The electron spin-orbit interaction breaks the degeneracy of states with non-zero angular momentum, contributing to the fine structure splitting of spectral lines [19]; 3P splits into three states, 3P_0 , 3P_1 and 3P_2 . Figure 2.1 shows how the five sublevels of the metastable 3P_2 state vary in an external magnetic field.

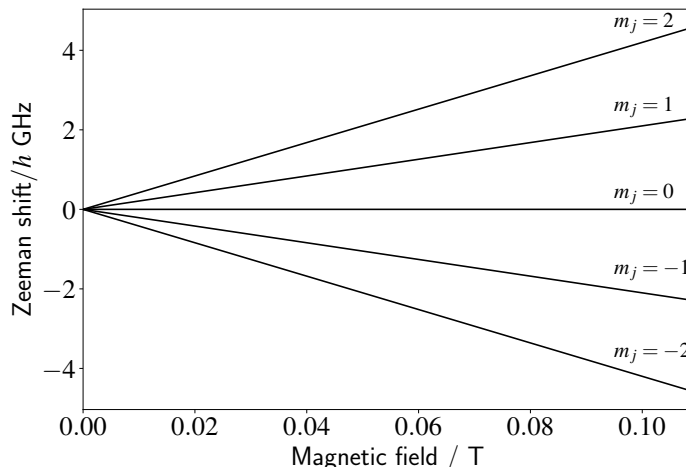


Figure 2.1: Zeeman splitting of energy levels for Ar 3P_2 .

If an atom possesses non-zero nuclear spin \mathbf{I} , the situation is different, and hyperfine structure must be considered. The nucleus has a magnetic moment $\boldsymbol{\mu}_I$:

$$\begin{aligned}\boldsymbol{\mu}_I &= g_I \frac{e}{2m_p} \mathbf{I} \\ &= g_I \mu_N \frac{\mathbf{I}}{\hbar},\end{aligned}\tag{2.1.7}$$

where g_I is the nuclear g-factor, and $\mu_N = e\hbar/2m_p$ is the nuclear magneton. Given that the Bohr and nuclear magnetons differ only in that the former contains the electron mass m_e and the latter the proton mass m_p , the nuclear dipole moment can be expressed as:

$$\boldsymbol{\mu}_I = g_I \frac{m_e}{m_p} \mu_B \mathbf{I}.\tag{2.1.8}$$

This of course means that μ_I is smaller than μ_B by a factor of m_p/m_e , and so the energy differences in hyperfine structure are smaller than those in fine structure. In the case neglecting nuclear spin the total angular momentum was $\mathbf{J} \equiv \mathbf{L} + \mathbf{S}$, whereas now it is given by $\mathbf{F} \equiv \mathbf{I} + \mathbf{J}$, with the projection quantum number m_f .

Much of the work in this report discusses our proposed sympathetic cooling experiment, featuring atomic lithium and molecular calcium hydride. Figure 2.2 shows the Zeeman splitting of ground-state ${}^7\text{Li}$. This has nuclear spin $I = 3/2$ and electron angular momentum $J = 1/2$, giving total angular momentum $F = 1$ or 2 .

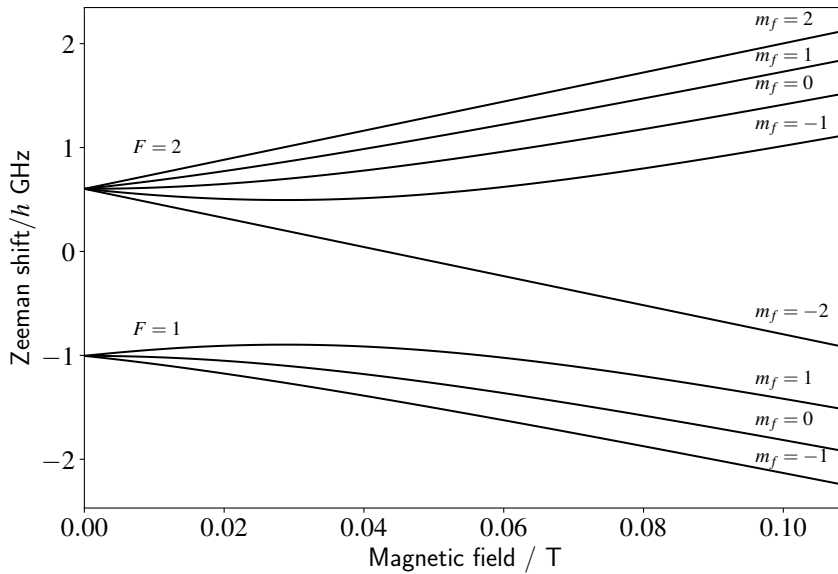


Figure 2.2: Zeeman splitting of energy levels for ${}^7\text{Li } 2S_{1/2}$.

Molecules also undergo energy level changes in a magnetic field, and many of the same components as in the atomic case are present - *e.g.*, the spin and angular momentum of the electron, and nuclear spin. However, rotational and vibrational terms complicate matters. For many situations a simplified molecular Hamiltonian can often be used to provide results at a required level of accuracy [20]. The electronic ground state of calcium hydride is $X^2\Sigma^+$ which has zero electronic orbital angular momentum, total electron spin of $1/2$, and total nuclear spin of $1/2$. The total angular momentum of the molecule is $\mathbf{F} \equiv \mathbf{J} + \mathbf{I}$ as before, however in this case $\mathbf{J} = \mathbf{N} + \mathbf{S}$, where \mathbf{N} is a term arising from the coupling of \mathbf{L} with the nuclear rotational angular momentum \mathbf{R} .

The simplified, effective Hamiltonian applying to this molecule contains components arising due to molecular rotation, corrections for centrifugal distortion, a coupling of the electron spin and molecular rotation, and a Zeeman Hamiltonian. Figure 2.3 shows the effect of an applied magnetic field on the energy levels of the rotational ground and first excited states $N = 0$ and 1 for CaH, for the vibrational ground state. This diagram was produced by L. McArd [2]; for further details on the model being used see also [20, 21].

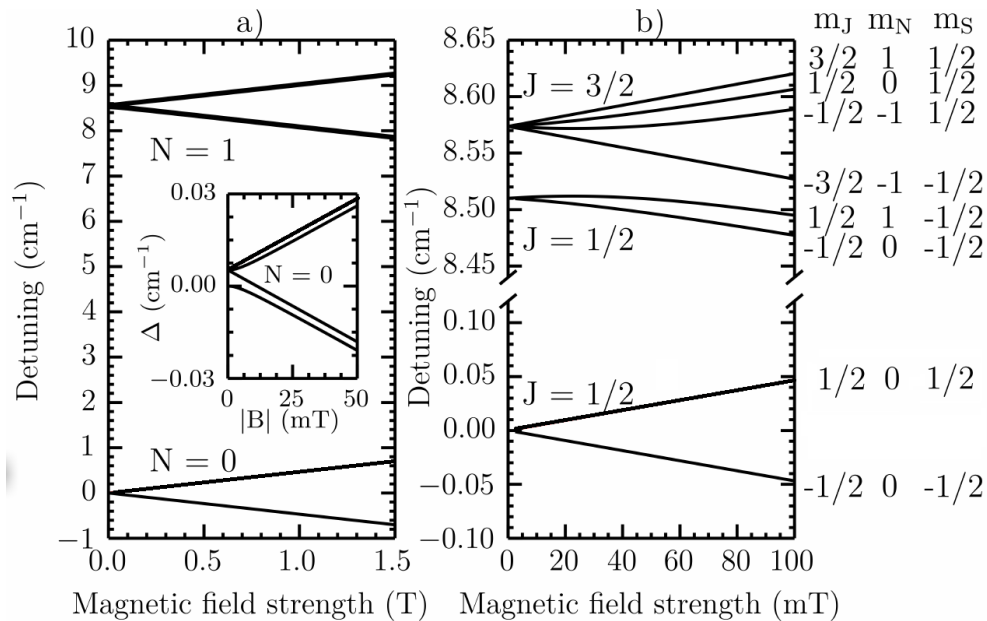


Figure 2.3: Magnetic field dependence of the energy levels of CaH in electronic ground state $X^2\Sigma^+$. a): Rotational states $N = 0$ and 1 , inset, hyperfine splitting of $N = 0$. b): Zoomed-in view showing zero-field splitting of the rotational states, and Zeeman-shifting of the sublevels described by the m_j quantum number. (This image courtesy L. McArd [2]).

2.2 Laser cooling

Einstein showed that radiation is exchanged in discrete bundles [22], and the quantised nature of the momentum of light was subsequently demonstrated by Compton [23]. The first observation of the mechanical action of light on matter was performed by Frisch [24] in 1933 when he deflected a beam of atomic sodium with light from a sodium lamp. Following the invention of the laser, Ashkin *et al.* [25] performed the first experiments on radiation pressure arising from laser light. When applied to atoms, a sufficiently intense laser resonant with an atomic transition saturates the transition, such that the rate of absorption approaches that of spontaneous emission, producing much stronger light forces than the earlier experiments.

Qualitatively, one can imagine an atom moving through space into a laser, propagating in the opposite direction. On absorbing a photon from the beam, the atom is excited, but also loses momentum equal to that of the photon. On spontaneous de-excitation the atom will regain this momentum, but due to the isotropic nature of the emission, in a random direction. Over repeated cycles the atom will clearly lose net momentum in the direction it was originally moving in. This naturally leads to the mechanism of Doppler cooling as proposed by Wineland and Dehmelt [26] and Hänsch and Schawlow [27]; by detuning the laser to the red side of the cooling transition, the probability of this interaction can be made to be velocity-dependent. By applying an inhomogeneous magnetic field that varies appropriately along the axis of propagation of a beam of atoms, the energy level of the cooling transition can be Zeeman-shifted to stay resonant as the atoms slow down - this is the operating mechanism of the Zeeman slower [9].

If these cooling lasers are applied from both directions on each Cartesian axis a full three-dimensional cooling effect known as ‘optical molasses’ is achieved. (Although cooled, atoms can still migrate out of this region, so a trapping force is often also applied - we shall return to this later).

2.3 Magnetic confinement

Even simple molecules can have very complicated internal energy levels due to the interaction between the constituent atoms and their additional rotational and vibrational degrees of freedom, so that they cannot be operated upon by a Zeeman slower [9]. The mechanical ac-

tion on neutral particles by magnetic fields was demonstrated long ago by Stern and Gerlach [28], and subsequently used in magnetic traps [29] and Zeeman decelerators [14].

In an inhomogeneous magnetic field \mathbf{B} a magnetic dipole experiences a force \mathbf{F} :

$$\begin{aligned}\mathbf{F} &= -\nabla U \\ &= \nabla(\boldsymbol{\mu} \cdot \mathbf{B}).\end{aligned}\tag{2.3.1}$$

For our case this gives:

$$F_z = -g_J \mu_B m_j \frac{\partial B}{\partial z}.\tag{2.3.2}$$

If m_j is negative the particle is in a high-field seeking state (HFS) - it has lower energy in a region of higher field strength. Positive values of m_j give the opposite, low-field seeking (LFS) states - these minimise their energy where the field is weaker. This means where there is an inhomogeneous field, the HFS states will fall ‘up’ the field gradient, and the LFS ‘down’ it. Obviously, there can be no field maximum in free space so only LFS states can be trapped.

A Zeeman decelerator utilises this effect. In construction it is a series of solenoids, with the particle beam directed along the axis. The propagating particles see an increase in magnetic field magnitude, effectively a potential hill which they must climb, but as the centre of the moving packet is about to pass through a coil and ‘roll back’ down the hill, the coil is switched off. Repeating this multiple times translates the average forward velocity of the sample down [16].

There are issues with this technique - there are only one set of coils for both longitudinal and transverse motion, meaning that the particle motion in these directions is coupled. Any particle sample has a spatial and velocity spread, and optimising the switching times for the coils to account for the leading and trailing edges is problematic, leading to losses. Our approach is to synthesise a true 3D moving potential, with separate components for longitudinal and transverse confinement [1, 2].

2.4 The Durham decelerator

The Carty group MTZD has three main components - the source chamber, decelerator stage, and the detection chamber, as shown in figure 2.4:

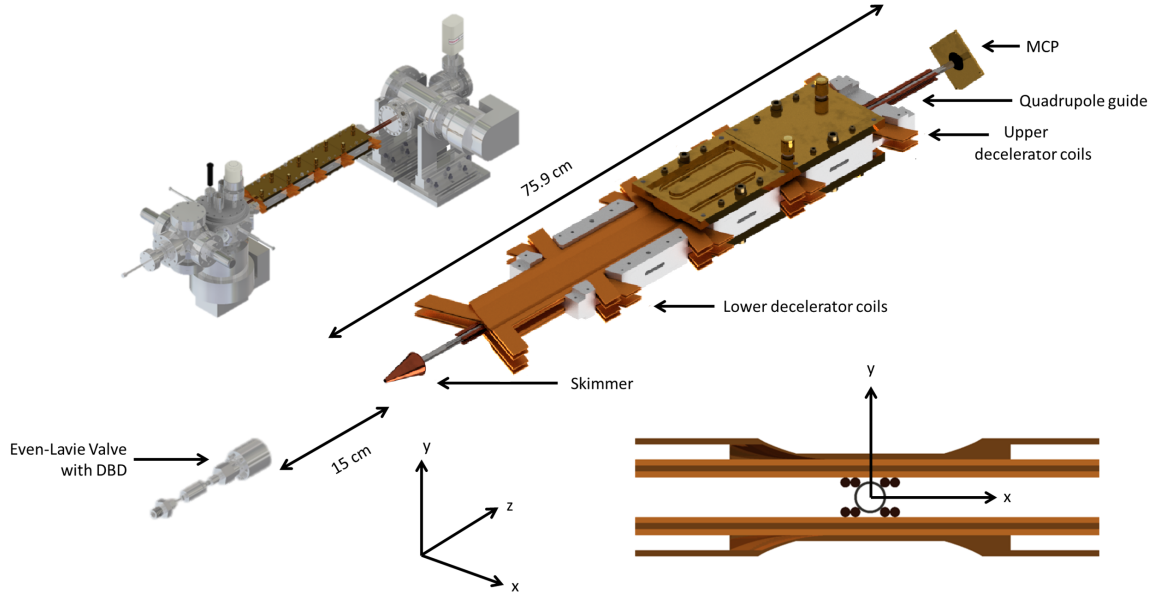


Figure 2.4: Carty group moving-trap Zeeman decelerator. Top left; source and detection chambers connected by delivery tube, with deceleration coils overlaid. Centre; valve, coils, cooling plates, quadrupole and detector. Bottom right; transverse section showing coils and quadrupole. (Image courtesy L. McArd).

Our experiment uses a pulse-type ‘Even-Lavie’ source [30]. This is a magnetically-actuated valve which produces pulses of duration on the order of $10 \mu\text{s}$. The valve also contains a dielectric-barrier discharge (DBD) system in the nozzle; this can be used to produce radical, metastable or ionised particles depending on the species involved. The DBD produces an electrical discharge between two electrodes surrounding a cylindrical insulator, via a series of RF pulses. In current work we are characterising our decelerator with argon, which must be energised to a metastable, low-field seeking state in order to be decelerated. (Of course, the excitation pulse can not selectively excite to particular states, and we should expect as many high-field seeking atoms to be produced as low-field seeking; these will be rapidly lost from the decelerator). In the case of argon it is necessary to engage the DBD even for non-guided transmission; the excitation pulse is required to give the atoms sufficient internal energy to trigger our microchannel-plate detector (MCP). The output pulses from the Even-Lavie valve undergo supersonic expansion [31], a skimmer removes the portion of the gas packet with high transverse velocities, and the remainder is delivered into the central

transport tube.

The decelerator stage is based on the design of Trimeche *et al.* [32]. The decelerator coils are helical and planar, and there are two pairs above and two pairs below the tube. Time-dependent DC current is supplied to the separate wire phases using H-bridge circuits controlled by dedicated electronics. This synthesises an AC current and thus a longitudinally travelling magnetic wave. This wave can be set to have a constant phase speed for constant velocity particle guiding or be ‘chirped’ down to decelerate the sample. Eight straight wires, two per corner, carry high-current DC pulses to produce a quadrupole field for transverse confinement. For further details on the design and construction of the decelerator see Mizouri [1] and McArd [2].

Finally, there is the detection chamber. This currently contains a microchannel plate detector (MCP) which allows a time-of-flight profile of the transported sample to be generated. In future this will be swapped for a quadrupole mass spectrometer.

The Liouville theorem [33] essentially states that conservative forces cannot produce real cooling, *i.e.* in the sense of phase-space compression. The MTZD allows the mean forward velocity of the gas packet to be translated down, but the internal temperature is not effected (in contrast with a Zeeman slower [9], in which the axial laser produces a dissipative force).

2.5 Magneto-optical traps

In section 2.2 the principle of laser-cooling in an ‘optical molasses’ apparatus was described. This method allows atoms to be cooled, but they can migrate out of the cooling region as there is no position-dependence to the effect. This is achieved in the magneto-optical trap (MOT), first demonstrated by Raab *et al.* [34] in 1987. The MOT also relies on counter-propagating lasers, detuned from resonance with a transition of the atom, but these lasers are circularly-polarised, and a quadrupole magnetic field gradient is superimposed with a pair of coils. This magnetic gradient does not confine the atoms using a Stern-Gerlach type effect (see section 2.3), but instead causes a position-dependence in the scattering forces they experience. The method discussed here works for any transition from a ground state with total angular momentum J_α to excited state $J_\beta = J_\alpha + 1$, but for simplicity we will consider $J = 0 \rightarrow J = 1$, which has excited states $m_j = -1, 0$, or 1 .

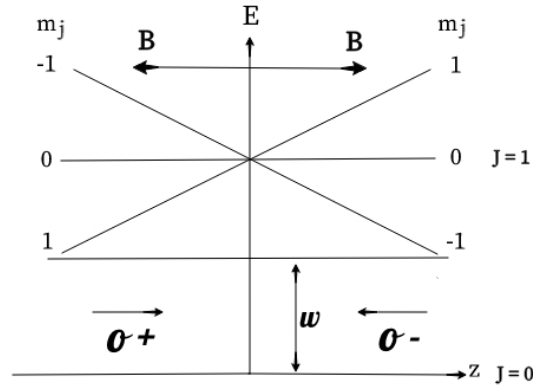


Figure 2.5: Operation of a MOT in one dimension for a $J = 0$ to $J = 1$ transition. The magnetic field \mathbf{B} varies linearly along the z -axis, splitting the energy of the excited-state sublevels and bringing them to resonance with the cooling lasers, of frequency ω . Circular polarisations σ^+ and σ^- clockwise and anti-clockwise with respect to space-quantisation axis z . (Note: ω and Zeeman shift not to scale).

Figure 2.5 shows how this works. The magnetic field breaks the degeneracy of the sublevels of $J=1$; in regions of positive z we have $B_z > 0$, therefore $m_j = -1$ decreases and $m_j = 1$ increases in energy (these are high- and low-field seeking states - see section 2.3). B_z is aligned in the opposite direction for $z < 0$ so the energy shifts of $m_j \pm 1$ are reversed.

A counter-propagating laser, red-detuned below the $J = 0 \rightarrow J = 1$ transition, is directed along the z -axis into the centre of the trap. The laser is circularly-polarised, with the beams travelling in the negative and positive x directions having σ^- and σ^+ polarisation, respectively. These polarisations impart angular momentum $\Delta m_j = -1$ and $+1$ respectively, so that atoms in the positive z region are closer to resonance with the beam moving in negative z , and vice-versa. This makes the scattering interaction between the atoms and the incident light field position dependent, adding a confining force to Doppler-cooling. Placing beams on the other Cartesian axes extends this scheme to three dimensions.

Although the details given here apply to a standard MOT setup with a quadrupole field produced by two coils in an anti-Helmholtz arrangement, we hope to achieve the same effect in a dodecapole, permanent magnet trap. Our proposed trap geometry is shown in chapter 3. Future work will simulate a MOT effect in this geometry. For further detail on the operation of a MOT see *e.g.* Foot [19].

2.6 Beyond laser cooling

Various methods are often jointly employed in producing ultracold atomic or molecular samples. As well as laser cooling, evaporative cooling is an important technique. This works in an exactly analogous way to evaporative losses from a hot cup of coffee; consider a sample of particles in thermal equilibrium - the energy of the population is being constantly redistributed through elastic collisions. As the fastest particles escape the average energy of the remaining sample is reduced - the high-energy tail of the Maxwell-Boltzmann distribution is cut off - but it is repopulated as a new equilibrium is reached. This new population will have a lower mean speed and a narrower spread of speeds, i.e. a lower temperature. This technique for trapped neutral atoms was first suggested by Hess [35] for hydrogen and then subsequently extended to alkali atoms by Petrich *et al.* [36]. This was instrumental in achieving the first Bose-Einstein condensate [37].

An additional technique is sympathetic cooling, which is again easy to understand in a qualitative way; two different populations exchange energy via elastic collisions - consider pouring cold milk into the aforementioned coffee. This was demonstrated by Myatt *et al.* [38]; they trapped a sample of ^{87}Rb containing a mixture of two different spin states, one of which was more strongly confined than the other. The less weakly-bound population lost energy via evaporative loss, and then cooled the more strongly-bound population via thermal contact.

Sympathetic cooling can also be combined with laser cooling - a species that can be laser-cooled is overlaid with one that cannot, and energy is therefore extracted from the latter via the former. This has been demonstrated for ions [39] and studies are underway to achieve this with molecules [40, 41]. Our goal is to sympathetically cool CaH molecules with laser-cooled Li atoms.

There is much more to consider regarding sympathetic cooling and our experimental goals, including the use of optical pumping and additional magnetic fields to suppress inelastic collisions and unwanted chemical reactions. This will be addressed in future work.

Chapter 3

Magnetic trap design

Magneto-optical traps are often built using a quadrupole field geometry, which can be produced using a pair of solenoids in an anti-Helmholtz configuration. Our proposed sympathetic cooling experiments require a different approach; we need a deep magnetic trapping potential to allow confinement of particle samples with significant temperatures, but a shallow gradient suitable for MOT in the centre. This novel field geometry is to be achieved using a combination of permanent magnets and solenoids (a trap with similar geometry was considered in Nohlman [42], see chapter 5). This chapter will describe these components, and the shape and nature of the trapping fields.

3.1 Trap components

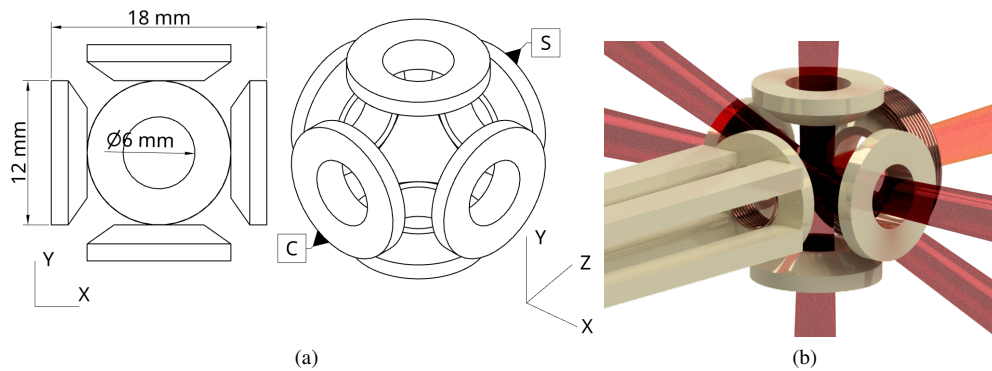


Figure 3.1: Magnetic trap / magneto-optical trap. (a), toroidal magnet dimensions and configuration. Face labelled 'c' contains 'cancellation' coil to 'open' the trap, face labelled 's' holds a 'slower' coil to provide a final stopping potential for the sample to be loaded. (b), rendered image showing magnets, coils and lasers for cooling / optical pumping for quantum state selection. This image courtesy L. McArd [2].

Two different views of the proposed trap apparatus are given in figure 3.1. The drawing on the left shows the six toroidal magnets, with a residual magnetization corresponding to grade N27 NdFeB. The inner diameter is 6 mm and the pole spacing 12 mm. The chamfer on the inner faces improves optical access without sacrificing too much trapping potential. The face in negative z as shown in figure 3.1 contains a cancellation coil, which carries a current

of 190 A to flatten the potential and effectively ‘open’ the trap. The opposite magnet has a larger ‘slower’ coil which produces the final stopping potential. The switching times and slower coil current settings are discussed in chapter 5. The rendered image on the right shows the complete assembly, with the quadrupole running up to the front face. The cancellation coil is inset into the bore of this magnet, and the slower coil can be seen wrapped around the opposite magnet. Cooling lasers are shown on the x - and y -axes; the corresponding z - component required for a 3D-MOT effect is provided by the diagonal beam (the beam obviously cannot be placed on z , which is the line of the decelerator). The beam shown entering along z is for optical pumping.

3.2 Trap depth

The depth of a magnetic trap is a measure of the strength of its confining potential. There are several ways to quantify this; for example, as the maximum speed of a single trapped particle, or as the maximum temperature of an ensemble of particles. A species-independent way to describe the trap depth is to simply give the minimum magnitude of the magnetic field at some distance from the centre of the trap.

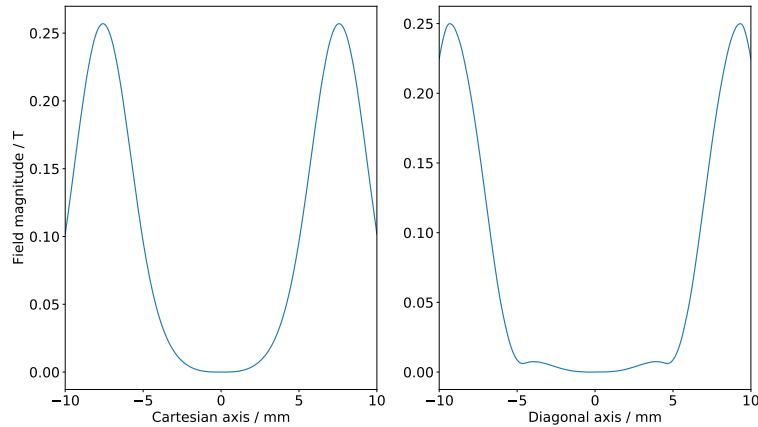


Figure 3.2: Magnetic trapping potential along a line through the MT-MOT. Left, along one of the Cartesian axes, right, along one of the diagonal axes.

Along the x -, y - and z -axes the trap depth is 0.257 T, at a distance from the centre of the trap $r = 7.5$ mm. This corresponds to the centre of the bore of one of the ring magnets, as shown in figure 3.2. Along the trap diagonals the potential has a broadly similar shape and depth, albeit at a slightly larger radial distance.

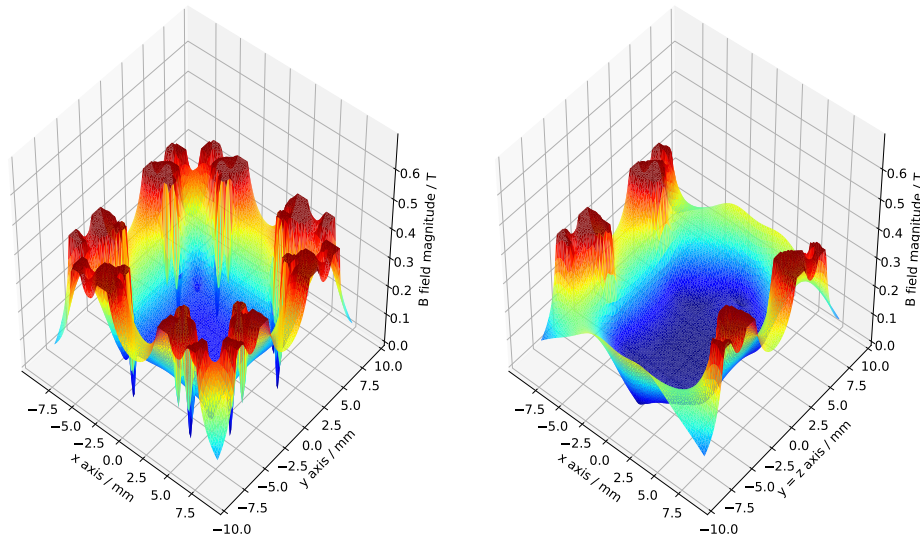


Figure 3.3: Magnetic trapping potential in a 2D slice through the MT-MOT. Left, the xy -plane, right, a rotation of 45° around the x -axis.

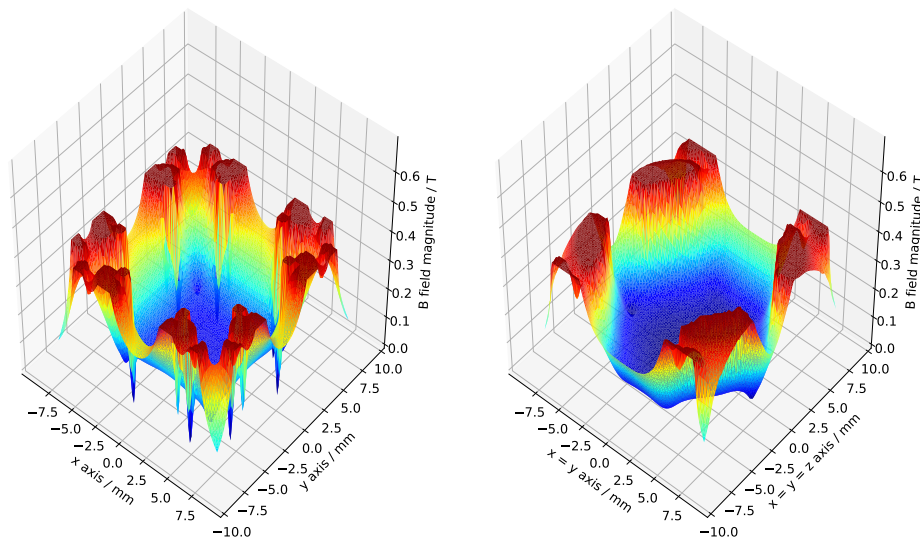


Figure 3.4: Magnetic trapping potential in a 2D slice through the MT-MOT. Left, the xy -plane, right, a rotation of 45° around both the x - and y -axes.

Figures 3.3 and 3.4 show two-dimensional cuts through the trap, in the xy -plane, the same plane then rotated at 45° around the x -axis, and then by 45° around the y -axis. Simulations show that 40% of the surface of a sphere of radius $r = 7.5$ mm in this field has $|\mathbf{B}| < 0.257$ T, and in fact for the xy -, yz - and xz -planes the depth at $r = 7.5$ mm is 0.113 T.

Simply looking at the field magnitude for various cuts through the trap is not a good way

to determine the actual trap depth for such a complicated field geometry. Instead, a Monte Carlo method was used, in which samples of Li atoms and CaH molecules with randomised positions and velocities were generated in the trap volume and allowed to evolve for some time. The depth of the trapping potential was then determined by equating the kinetic energy of the fastest moving particles that remained in the trap volume with their Zeeman energy, to give $v = \sqrt{2(\mu_B/m)B}$. This showed the trap to have an effective depth of 0.167 T. Further consideration of this will be given in chapter 5.

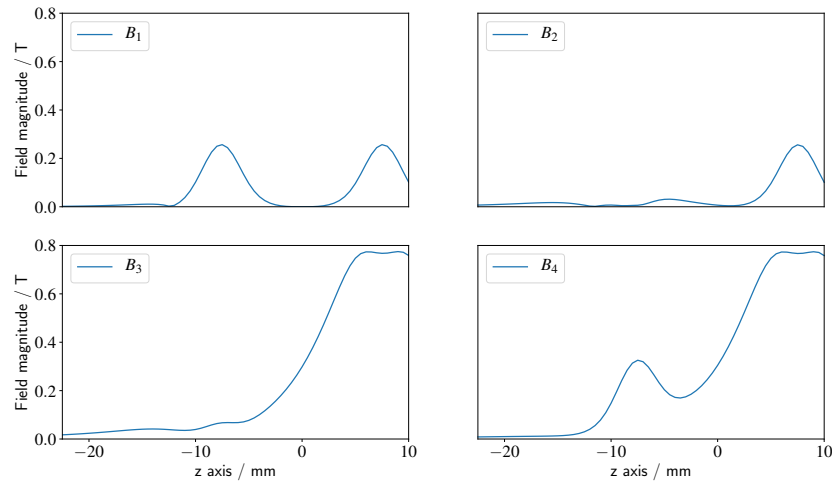
3.3 Trap fields

There are four different magnetic field configurations. All feature the permanent magnets and quadrupole guide with one, both, or neither of the coils, as defined below:

Table 3.1: Field configurations.

| Field name | Components |
|------------|--|
| B_1 | permanent magnets and quadrupole guide |
| B_2 | permanent magnets, quadrupole guide and cancellation coil |
| B_3 | permanent magnets, quadrupole guide, cancellation and slower coils |
| B_4 | permanent magnets, quadrupole guide and slower coil |

The intended mode of operation is that the approaching particle sample from the decelerator encounters the leading magnet potential shown in B_1 , removing kinetic energy from the leading part of the packet. The cancellation coil kicks in to ‘open’ the trap in B_2 , then the slower coil in B_3 provides the final stopping potential. In B_4 the cancellation coil switches off to ‘close’ the trap, before too much of the packet can bounce back out. Finally the slower shuts off to return to the permanent magnet only state, B_1 . Figure 3.5 shows the field magnitude along the z -axis for the different regimes. The current in the cancellation coil is fixed by the requirement to just nullify the front magnet, whereas the slowing potential is an adjustable parameter, as are the switching times.

Figure 3.5: Trapping fields on z -axis, slower coil at 460 A.

The relatively flat bottom and steep sides of the trapping potential can be seen, but the field geometry is much more complex than figure 3.5 suggests - figure 3.6 shows the field magnitude for the yz -plane. The quadrupole can be clearly seen aligned along z , with the cancellation coil ‘opening’ the trap, and the slower coil providing the final stopping potential. This illustrates the need to move beyond 1D simulations on the propagation axis.

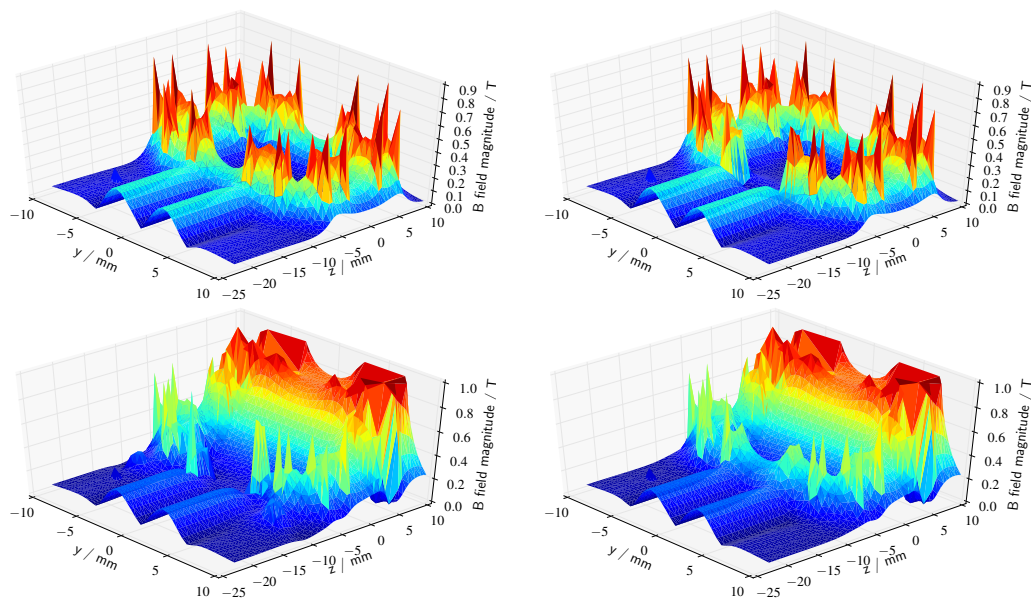
Figure 3.6: Trapping fields in yz -plane, slower coil at 460 A. Upper left, B1, upper right, B2, lower left, B3, lower right, B4.

Figure 3.7 shows a zoomed-in plot of the B -field magnitude along z at the centre of the trap. Theory suggest that the relatively shallow gradient in the region of about $|z| < 0.7$ mm should be suitable for achieving MOT.

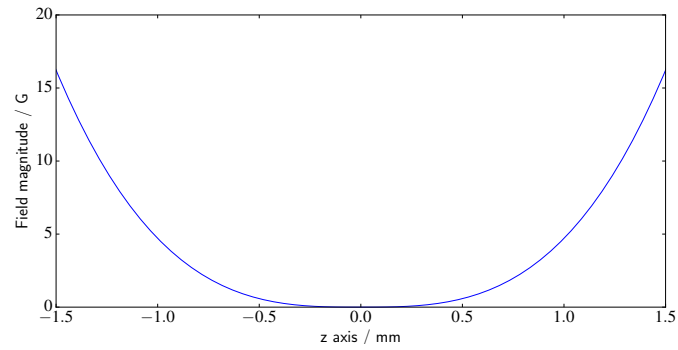


Figure 3.7: Close-up of trapping fields on z -axis. MOTs are generally built in quadrupole traps and it can be seen that the geometry here is different. However, theory suggests that it should be achievable. This remains to be tested in future work.

Chapter 4

Simulation methodology

Our group utilised computer simulation in the design of the Zeeman decelerator, and in interpreting the experimental results produced by it. In the current work, the software methods previously used have been extensively modified and extended to the design of the proposed magnetic trap. In this section the methods used are described.

4.1 Field interpolation - spline

To simulate particle motion we need to be able to determine the instantaneous force acting on each due to the field gradient. It is possible to calculate the field due to a flow of current on the fly, but this is CPU intensive and slow - this was a particular problem in the decelerator simulations. Some field layouts have an analytic solution allowing rapid field calculation [43] but due to the nature of our trap design this was not feasible.

Various software packages exist for modelling magnetic fields using finite-element analysis [44] or boundary integral methods [45]. The solutions are output as a grid of components, which can be interpolated in order to determine the field at arbitrary coordinates. For the work in this report we modelled the MT-MOT in the Radia software package [45]. The balance between speed of interpolation and accuracy is determined by the choice of grid spacing and interpolation algorithm. In one-dimensional simulations the spline method is fast and effective - this uses cubic piecewise polynomials to draw a curve between data points and return the value and derivative of the interpolated variable [46]. Splines are not susceptible to the problems in other high-degree polynomial methods involving oscillations between points, and are included in the Scientific Python library 'scipy.interpolate' [47], making development fast and straightforward.

4.2 Field interpolation - tricubic

For three-dimensional simulations we use the well-known tricubic interpolator. This can be implemented as three one-dimensional problems (*cf.* Kadosh *et al.* [48]) but we follow the method of Lekien and Marsden [49] which is inherently three-dimensional. It is also a local, rather than global, interpolation scheme, which allows irregular grids and avoids global propagation of sampling errors.

The interpolation volume is defined by the grid of field components produced by the modelling software. This volume is comprised of cuboid elements whose corners are the grid points. Considering any one of these elements, the B field at an arbitrary point inside it is given by the following sum (note that B here is the *magnitude* of the field, as that is all that the Zeeman potential depends on):

$$B(x, y, z) = \sum_{i,j,k=0}^N a_{ijk} x^i y^j z^k. \quad (4.2.1)$$

The order N is determined by the required degree of smoothness of the approximation. B and its first derivatives:

$$B, \frac{\partial B}{\partial x}, \frac{\partial B}{\partial y}, \frac{\partial B}{\partial z}, \quad (4.2.2)$$

must be continuous at each corner to satisfy C^1 parametric continuity. This gives 32 constraints, so N must be at least 3. Setting $N = 3$ there are 64 coefficients a_{ijk} for each element - the remaining constraints are given by requiring continuity of further derivatives. It can be shown [49] that the only valid set of functions that are independent of set (4.2.2) and are isotropic under coordinate rotation are:

$$\frac{\partial^2 B}{\partial x \partial y}, \frac{\partial^2 B}{\partial x \partial z}, \frac{\partial^2 B}{\partial y \partial z}, \frac{\partial^3 B}{\partial x \partial y \partial z}. \quad (4.2.3)$$

We place the coefficients a_{ijk} in a vector \mathbf{a} with components:

$$a_{ijk} = a_{1+i+4j+16k} \quad \text{for } i, j, k \in \{0, 1, 2, 3\}, \quad (4.2.4)$$

and add the functions given in (4.2.2) and (4.2.3) for each corner $c_1 \dots c_8$ into a vector \mathbf{f} :

$$f_i = \begin{cases} B(c_i) & \text{for } 1 \leq i \leq 8 \\ \frac{\partial B}{\partial x}(c_{i-8}) & \text{for } 9 \leq i \leq 16 \\ \dots & \\ \frac{\partial^3 B}{\partial x \partial y \partial z}(c_{i-56}) & \text{for } 57 \leq i \leq 64, \end{cases} \quad (4.2.5)$$

the vectors can be related by the expression:

$$M\mathbf{a} = \mathbf{f}, \quad (4.2.6)$$

where M is a 64×64 matrix, easily calculable [49]. The matrix is invertible, so:

$$\mathbf{a} = M^{-1}\mathbf{f}. \quad (4.2.7)$$

B at each grid point is known, and the associated derivatives \mathbf{f} are calculated via finite difference methods [50], allowing the coefficients a_{ijk} to be determined. Interpolation of B for an arbitrary point (x, y, z) is given by:

$$B = \mathbf{a} \cdot (\mathbf{x} \cdot \mathbf{y} \cdot \mathbf{z}), \quad (4.2.8)$$

and ∇B with:

$$\nabla B = \begin{pmatrix} \mathbf{a} \cdot \left(\frac{\partial}{\partial x} \mathbf{x} \cdot \mathbf{y} \cdot \mathbf{z} \right) \\ \mathbf{a} \cdot \left(\mathbf{x} \cdot \frac{\partial}{\partial y} \mathbf{y} \cdot \mathbf{z} \right) \\ \mathbf{a} \cdot \left(\mathbf{x} \cdot \mathbf{y} \cdot \frac{\partial}{\partial z} \mathbf{z} \right) \end{pmatrix}. \quad (4.2.9)$$

Defining O_i as a matrix of ones of length i and \otimes as the Kronecker product, the vectors \mathbf{x} , \mathbf{y} and \mathbf{z} are given by:

$$\begin{aligned} \mathbf{x} &= O_{16} \otimes (1, x, x^2, x^3)^T \\ \mathbf{y} &= O_4 \otimes (1, y, y^2, y^3)^T \otimes O_4 \\ \mathbf{z} &= (1, z, z^2, z^3)^T \otimes O_{16}, \end{aligned} \quad (4.2.10)$$

with partial derivatives:

$$\begin{aligned}
 \frac{\partial}{\partial x} \mathbf{x} &= O_{16} \otimes (0, 1, 2x, 3x^2)^T \\
 \frac{\partial}{\partial y} \mathbf{y} &= O_4 \otimes (0, 1, 2y, 3y^2)^T \otimes O_4 \\
 \frac{\partial}{\partial z} \mathbf{z} &= (0, 1, 2z, 3z^2)^T \otimes O_{16}.
 \end{aligned}
 \tag{4.2.11}$$

For a given B field layout we calculate the matrix of coefficients a_{ijk} for each element in the volume. For example; a cubic volume with coordinates $-10 \text{ mm} \leq [x,y,z] \leq 10 \text{ mm}$ with a grid spacing of 0.5 mm has 41 points on each axis, and the output file has $41^3 = 68921$ rows. These grid points define $40^3 = 64000$ cubic elements. Each element has values of the components in sets (4.2.2) and (4.2.3) at the corners giving 64 coefficients a_{ijk} . The derivatives of \mathbf{B} cannot be found for points at the edges, which shrinks the interpolation volume so that there are $38^3 = 54872$ elements. The set of coefficients a_{ijk} is therefore a 54872×64 matrix.

When interpolating the field at an arbitrary point, the software determines the appropriate coefficients to load from the matrix and assembles the field magnitude and derivatives. For any given field configuration a unique matrix is calculated and saved to file; this can be loaded as required to save redundant computation. Our simulations use an adjustable discrete timestep; for each step the effective force felt by the simulated particle is determined by combining the gradient with the mass of the particle and the Bohr magneton. The stepwise solution of the equations of motion is discussed in the following sections.

The tricubic interpolator was initially implemented in Python for our group by Ulrich Krohn for use in simulations of the decelerator. We have recently achieved an order of magnitude increase in the speed of our software by carefully re-writing the code to improve efficiency - particularly in reducing the reliance on Python list comprehension, and reducing I/O operations by handling larger blocks of data at a time. We have additionally added multiprocessor support to allow the code to run on the university supercomputer cluster.

4.3 Numerical methods - Runge-Kutta

Solving the motion of a body through a region containing an inhomogeneous potential is complicated if there is no analytical solution to the potential. The obvious approach is to break the simulation into small discrete steps, and calculate the change in position and velocity at each step. A first choice is to use the Newtonian equations of motion relating initial and final velocities u and v , acceleration a , distance s and time t :

$$v = u + at, \quad (4.3.1)$$

$$s = ut + \frac{at^2}{2}. \quad (4.3.2)$$

Any numerical method will introduce errors, and the errors arising from this method are unacceptably high. The decelerator project utilised a fourth-order Runge-Kutta algorithm [51] (we will attempt to quantify the errors in a later section). Runge-Kutta are a family of numerical methods for approximating ordinary differential equations - the simplest is the well-known Euler method. RK4 works as follows; if we wish to model q , some function of time t , whose rate of change \dot{q} is a known function of q and t :

$$\dot{q} = f(t, q), \quad (4.3.3)$$

and initial conditions:

$$q(t_0) = q_0, \quad (4.3.4)$$

for some time step h , we get q_{n+1} , the approximation to the unknown $q(t_{n+1})$:

$$q_{n+1} = q_n + \frac{h}{6}(k_1 + 2k_2 + 2k_3 + k_4), \quad (4.3.5)$$

$$t_{n+1} = t_n + h, \quad (4.3.6)$$

where:

$$k_1 = f(t_n, q_n), \quad (4.3.7)$$

$$k_2 = f\left(t_n + \frac{h}{2}, q_n + \frac{h}{2}k_1\right), \quad (4.3.8)$$

$$k_3 = f\left(t_n + \frac{h}{2}, q_n + \frac{h}{2}k_2\right), \quad (4.3.9)$$

$$k_4 = f(t_n + h, q_n + hk_3). \quad (4.3.10)$$

We apply this technique in the form of six simultaneous cases, three relating position to velocity and three relating velocity to acceleration, along the Cartesian axes. They are not independent and must be solved in sequence. (*cf.* Voesenek [52] for an analogous implementation in orbital motion.)

The spatial and velocity coordinates of our particle sample are given in a $6 \times N$ matrix where N is the sample size. At some time $t = n$ the i th row contains the phase-space coordinates for the i th particle, shown here as the array p_n :

$$p_n = [x_n, y_n, z_n, v_{x,n}, v_{y,n}, v_{z,n}]. \quad (4.3.11)$$

To calculate the coefficients k the acceleration a is required. Querying the tricubic interpolator at (x, y, z) gives the field gradient $\left(\frac{\partial B_x}{\partial x}, \frac{\partial B_y}{\partial y}, \frac{\partial B_z}{\partial z}\right)$, related to the effective force by equation (2.3.2); combining these with the particle mass gives the acceleration components (a_x, a_y, a_z) .

$$k_1 = [v_{x,n1}, v_{y,n1}, v_{z,n1}, -a_{x,n1}, -a_{y,n1}, -a_{z,n1}]. \quad (4.3.12)$$

Incrementing p with the timestep h :

$$\begin{aligned} p_{n2} &= p_n + \frac{h}{2}k_1 \\ &= [x_{n2}, y_{n2}, z_{n2}, v_{x,n2}, v_{y,n2}, v_{z,n2}]. \end{aligned} \quad (4.3.13)$$

We use the interpolator at (x_{n2}, y_{n2}, z_{n2}) to obtain a_{n2} . Proceeding as before gives k_2 and p_{n3} :

$$k_2 = [v_{x,n2}, v_{y,n2}, v_{z,n2}, -a_{x,n2}, -a_{y,n2}, -a_{z,n2}], \quad (4.3.14)$$

$$p_{n3} = p_n + \frac{h}{2}k_2, \quad (4.3.15)$$

And so on for k_3 and k_4 . Finally the result for p_{n+h} is assembled:

$$p_{n+h} = p_n + \frac{h}{6}(k_1 + 2k_2 + 2k_3 + k_4). \quad (4.3.16)$$

As with the interpolator software, we have been able to achieve significant performance increases through optimisation. The example given here deals with a single particle from the simulated distribution, but our code now handles the entire sample at each step using matrices - in Python, this is much more efficient than listwise iteration. For simulations involving more than one particle species, a matrix containing the relevant mass details *etc.* is assembled initially, which can be rapidly combined with the gradient at each call of the interpolator. This is faster than handling multiple cases separately.

4.4 Numerical methods - velocity Verlet

The Runge-Kutta method as previously discussed was extensively used in the decelerator project, and improved for the current work. Another numerical method for solving Newtonian motion is the Velocity Verlet algorithm [53], which is often used in molecular dynamics simulations [54] - this was investigated for suitability, as it offered the possibility of lower processing overheads.

For a particle with position vector $r(t)$ and a time step h , the basic Verlet algorithm starts from a Taylor expansion:

$$r(t+h) = r(t) + h \frac{dr(t)}{dt} + \frac{h^2}{2} \frac{d^2r(t)}{dt^2} + \frac{h^3}{6} \frac{d^3r(t)}{dt^3} + \mathcal{O}(h^4), \quad (4.4.1)$$

and:

$$r(t-h) = r(t) - h \frac{dr(t)}{dt} + \frac{h^2}{2} \frac{d^2r(t)}{dt^2} - \frac{h^3}{6} \frac{d^3r(t)}{dt^3} + \mathcal{O}(h^4), \quad (4.4.2)$$

which combine to give:

$$\begin{aligned} r(t+h) &= 2r(t) - r(t-h) + h^2 \frac{d^2r(t)}{dt^2} + \mathcal{O}(h^4) \\ &= 2r(t) - r(t-h) + h^2 a(t) + \mathcal{O}(h^4), \end{aligned} \quad (4.4.3)$$

with error term of order $\mathcal{O}(h^4)$ - we shall come back to this. This method requires storing two sets of position data in memory and makes no explicit use of velocity, as the first- and third-order derivatives cancel. It can instead be developed into the velocity Verlet algorithm [55]:

$$r(t+h) = r(t) + hv(t) + h^2 a(t), \quad (4.4.4)$$

$$v(t+h) = v(t) + \frac{a(t) + a(t+h)}{2}. \quad (4.4.5)$$

This was implemented as follows; as for RK4, we have an array p_n corresponding to the coordinates of one particle from our sample:

$$p_n = [x_n, y_n, z_n, v_{x,n}, v_{y,n}, v_{z,n}], \quad (4.4.6)$$

and we have returned the field gradients $\left(\frac{\partial B_x}{\partial x}, \frac{\partial B_y}{\partial y}, \frac{\partial B_z}{\partial z} \right)$ from the tricubic interpolator, from which we get the acceleration, a_n . This allows us to calculate the position and interim velocity change:

$$p_{n2} = [x_{n+h}, y_{n+h}, z_{n+h}, v_{x,n2}, v_{y,n2}, v_{z,n2}] = \left\{ \begin{array}{l} x_n + hv_{x,n} - h^2/2a_{x,n} \\ y_n + hv_{y,n} - h^2/2a_{y,n} \\ z_n + hv_{z,n} - h^2/2a_{z,n} \\ v_{x,n} - h/2a_{x,n} \\ v_{y,n} - h/2a_{y,n} \\ v_{z,n} - h/2a_{z,n} \end{array} \right\}^T. \quad (4.4.7)$$

The interpolator is then queried for the point $(x_{n+h}, y_{n+h}, z_{n+h})$ to get the new acceleration components a_{n2} , and we complete the iteration:

$$p_{n+h} = [x_{n+h}, y_{n+h}, z_{n+h}, v_{x,n+h}, v_{y,n+h}, v_{z,n+h}] = \left\{ \begin{array}{l} x_{n+h} \\ y_{n+h} \\ z_{n+h} \\ v_{x,n+h} - h/2a_{x,n2} \\ v_{y,n+h} - h/2a_{y,n2} \\ v_{z,n+h} - h/2a_{z,n2} \end{array} \right\}^T. \quad (4.4.8)$$

Again, although this example has shown how our code iterates the coordinates of one particle, in actual implementation it deals with the entire sample in matrix form.

Comparing the merits of the Runge-Kutta and Verlet integrators is not straightforward. Although estimates can be made of the relevant errors expected to accumulate in the two algorithms, simply comparing the outputs of two otherwise-identical simulations was not very instructive. Velocity Verlet uses fewer calculations and calls to the interpolator than Runge-Kutta *per iteration*, but Runge-Kutta can operate with a larger timestep at the same precision. In the following sections some attempts to quantify these differences are given.

4.5 Numerical integrator errors

The RK4 method has total accumulated error on the order of $\mathcal{O}(h^4)$ where h is the timestep [56]. In order to quantify the relative errors arising from RK4 and SUVAT methods, we define a simple case that can be directly solved by integration. For a one-dimensional motion in z where the acceleration is a function of position, $a(z)$, it is straightforward to relate velocity v_z to $a(z)$ and time t to v_z :

$$\frac{1}{2}v_z^2 = \int a(z) dz, \quad (4.5.1)$$

$$t = \int \frac{1}{v_z} dz. \quad (4.5.2)$$

Defining $a(z) = 4z$, and initial conditions $t_0 = z_0 = 0$, $v_0 = 1 \text{ m s}^{-1}$, leads to:

$$z = \frac{\sinh(2t)}{2}, \quad (4.5.3)$$

$$v_z = \sqrt{1 + \sinh^2(2t)}. \quad (4.5.4)$$

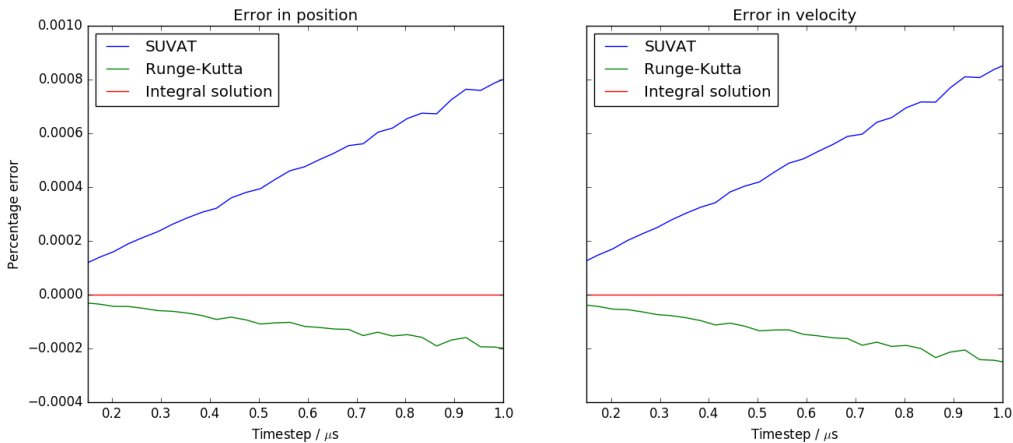


Figure 4.1: Errors in SUVAT and Runge-Kutta methods for solving motion in a non-uniform field.

Figure 4.1 shows the output of a script that compares the results of SUVAT and RK4 with the output of equations 4.5.3 and 4.5.4. For a given timestep the error arising from RK4 is

much smaller than that from the SUVAT method, however this comparison does not consider the amount of CPU time taken for each method.

In discussing the Verlet algorithm, we noted that the two components each have an error term of order $\mathcal{O}(h^4)$, which combine to make the method of overall second order. It seems clear that the Runge-Kutta method will give more exact results, but to try and clarify this we repeated the test from the previous section, this time directly comparing the RK and VV algorithms to our test case, as shown in figure 4.2:

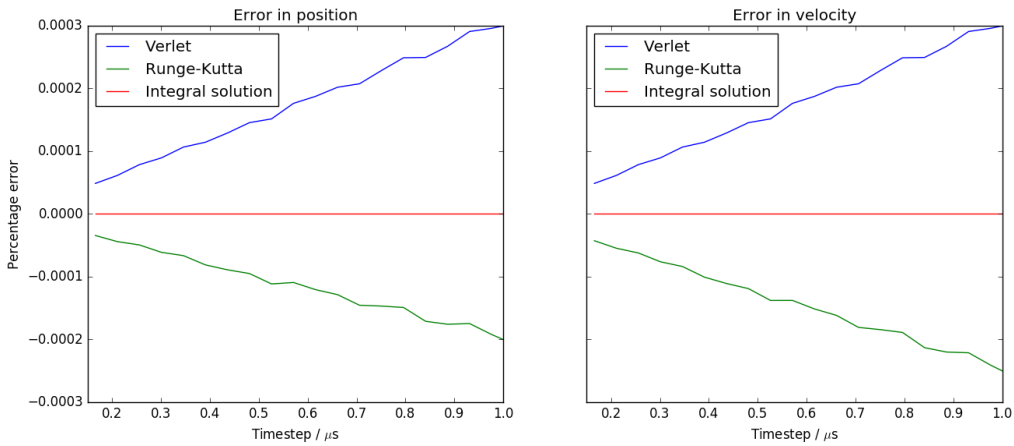


Figure 4.2: Errors in Velocity-Verlet and Runge-Kutta methods for solving motion in a non-uniform field.

The differences are not as large as when comparing Runge-Kutta to the Newtonian equations, as expected. At time steps in the region of 10^{-7} s the overall errors are very close, and even over the hundreds of thousand of time steps used in our simulations, the outputs were very similar. The Verlet algorithm was for this reason deemed suitable for use when we needed to perform many simulation runs to sweep the parameters of our trap design, and speed of completion was more important than absolute precision. Promising sets of design parameters were followed up with Runge-Kutta based Monte Carlo simulations. Chapter 5 gives the results of these simulations.

Numerical integration methods are often implemented with a variable step size [51], *e.g.* the Fehlberg method [57]; the simulation software dynamically adjusts the timestep in order to minimise run time whilst maintaining a target accuracy. This could be done with our simulations for a single particle, but for the heavily optimised way in which we deal with an ensemble of particles at each run this would not work - due to the strongly varying shape of

the potential we are modelling, the different parts of the simulated molecular cloud would not require the same timestep to maintain accuracy. Returning to dealing with the particles individually would slow the overall simulation down by a much greater degree than any gains that were made. However, this would provide a better way to assess the efficiency of different algorithms in terms of actual CPU cycles, even without a ‘true’ analytical solution against which to compare them. Future work will address this.

Chapter 5

Results

5.1 Trap loading - 1D simulation

A starting point for simulating the loading of the trap with a sample of particles from the decelerator was to consider the expansion of the gas packet that occurs as the decelerator releases it. This should only be a problem longitudinally - the laterally-confining quadrupole can be brought up to the trap (currently the quadrupole is wire, but we plan to move to a permanent magnet system soon). Bringing the decelerator coils into the trap chamber, however, would be problematic due to the need to make a vacuum seal around the wiring. An additional concern would be the heat load brought into the chamber.

Previous simulation work by the group gave likely phase-space distributions for a mixed sample of Li atoms and CaH molecules leaving the decelerator. These two species have different internal temperatures - typically 20 mK for CaH and 2 K for Li. One-dimensional simulations for a decelerator to trap distance $d_z = 200$ mm, packet mean velocity $v_z = 11.2$ m s⁻¹ and a packet width with a standard deviation $\sigma_z = 1$ mm, and neglecting interaction with the trap fields, were set up, using spline interpolation. The range of particle velocities was based around the one-dimensional Maxwell-Boltzmann distribution, relating standard deviation to temperature and mass:

$$\sigma_{v_z} = \sqrt{\frac{kT}{m}}. \quad (5.1.1)$$

This showed that on reaching the trap centre CaH had $\sigma_z \cong 33$ mm, and Li $\sigma_z \cong 840$ mm. Reconsidering how close the decelerator could be brought to the trap chamber, we repeated the simulations for $d_z = 14$ mm, giving $\sigma_z \cong 3$ mm and 14 mm for CaH and Li, respectively. Whilst more promising, the influence of the trapping fields still needed to be considered. The other immediately obvious factor in reducing the dispersion of the gas packet was to deliver it from the decelerator with a higher mean forward velocity - this would indeed reduce the unconfined time of flight, but it would be sure to make the trap loading process more difficult.

The simulator was rewritten to include the fields B_1 to B_4 as shown in figure 3.5. Preliminary results suggested some approximate values for the switching times, and the importance of a full 3D treatment to consider transverse fields and slower coil settings. For further discussion see McArd [2].

5.2 Trap loading - 3D simulation

Our aim is to move a packet of particles from the end of the decelerator and into the magnetic trap, ideally such that a zero average velocity is achieved with an average position at the trap centre. For the case of the ideal ‘synchronous particle’ moving along the longitudinal axis this is a simple matter of considering the magnetic field required to remove the kinetic energy. For a sample containing two species with different internal temperatures and masses this is much more problematic. 1D simulations showed a compromise situation where both species are loaded, albeit sub-optimally for each. Even if both packets are stopped within the trap, they will oscillate within it. We implemented 3D simulations of the process to gain a better understanding of it.

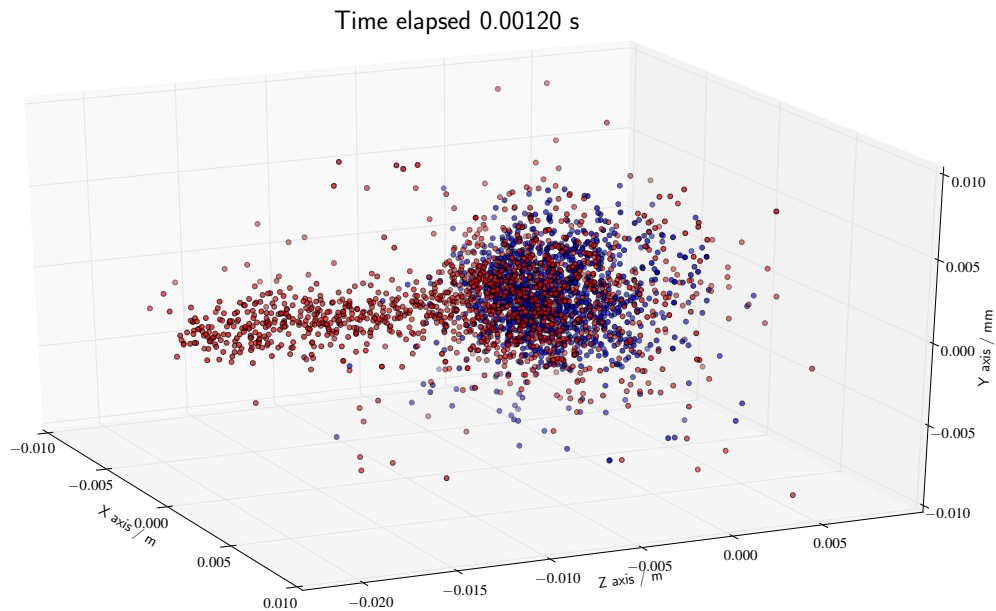


Figure 5.1: Snapshot of simulated trap loading process; at this stage the cancellation coil has ‘opened’ the trap and the final slowing coil is active. (Li atoms, red, CaH molecules, blue).

Figure 5.1 shows a plot of dual-species trap-loading simulation. The packet has entered the trap from the decelerator and encountered the final stopping potential of the slower coil. The internally hotter Li atoms (red) are more diffuse and a tail of them is still outside of the trap, although clearly still radially confined by the quadrupole. At this point in the simulation both the cancellation and slower coils will shortly deactivate, leaving only permanent magnet trapping forces.

As before, we interpolated the fields calculated in Radia, this time using the tricubic method. Particle motion was solved with the Verlet algorithm for initial sweeps of the trap parameters, with a detailed Runge-Kutta follow-up where needed. Probable phase-space distributions for the CaH and Li samples emerging from the decelerator, as found in previous decelerator Monte Carlo simulations, were used to build the starting distributions. Since no particle interactions were included, we were able to split each run into numerous processes allowing it to be parallelised on the supercomputer cluster.

Particles leaving the interpolation volume are classed as lost and removed from the distribution. The leaving direction (*i.e.* which face of the cuboid interpolation volume they leave from) is logged. It was found that the majority of particle loss occurs within 10 - 15 ms of the simulation starting, so the simulation runs were capped at 15 ms in most cases. (Loss mechanisms will be discussed in section 5.6). At the end of the run particles are classed as captured if they remain within 7.5 mm of the trap centre. (Subsequent work determined a better estimate of the trap depth - see section 3.2 - and so a better criterion could be used, *i.e.* particles with energies below the trap depth were classed as captured).

The switching in and out of the cancellation and slower coils at set times (see section 5.4) was implemented as a sharp transition between the B field profiles. Previous work by the group has estimated the actual rise times of the current in these coils to be in the tens of microseconds [2], which should be considered in future, more detailed work.

5.3 Trap loading - slower coil current

For the preliminary 1D simulations discussed earlier the slower coil had a current of 200 A, but it was desirable to determine what strength current would give the best loading results. Intuitively, one might expect that the current in the slower coil should be such that the field produced reinforces the field of the rear magnet, as shown in figure 5.2.

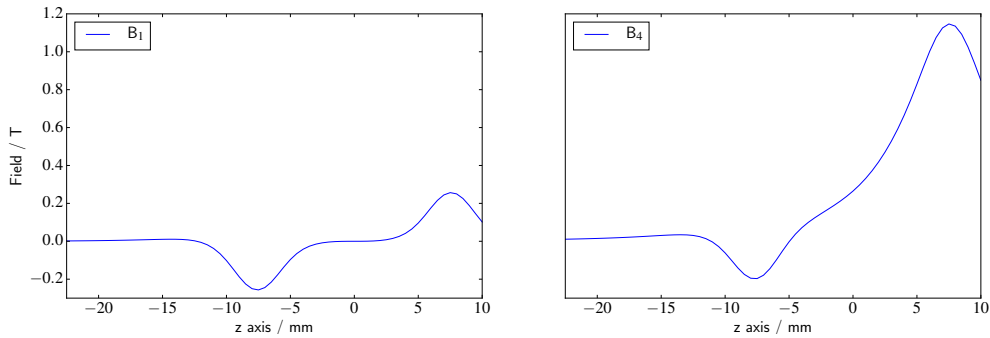


Figure 5.2: Trapping fields on z -axis. Left, trap only, right, slower coil at 460 A. Attention should be drawn to the distinction between figures 5.2 and 3.5, which showed the magnitude of the z -component.

This configuration, however, was found to be very lossy, because the lateral field is defocused in places. This is illustrated in figure 5.3, which shows the field magnitude in the xy -plane.

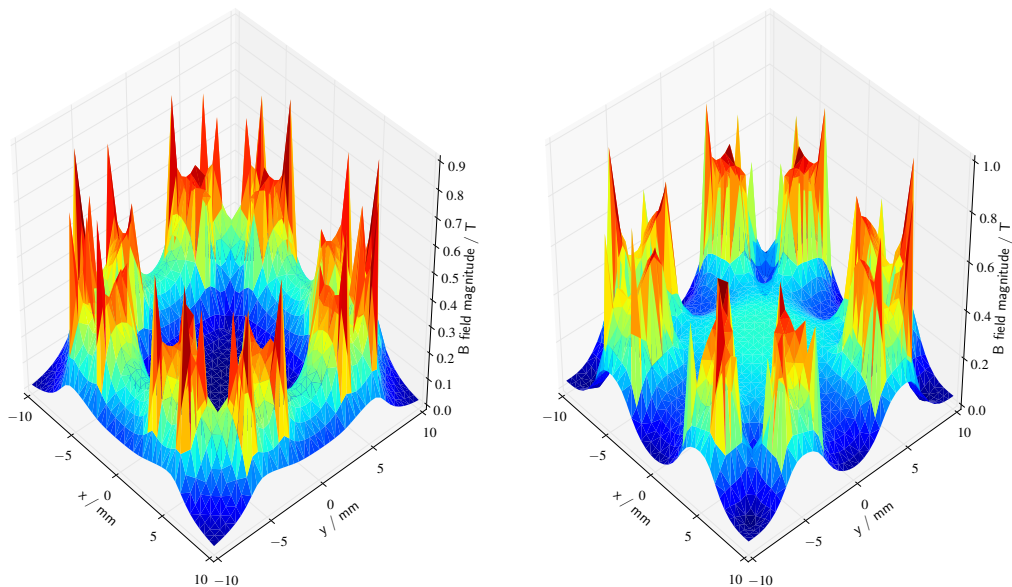


Figure 5.3: Trapping fields in xy -plane. Left, trap only, right, slower coil at 460 A.

Reversing the current flow, so that the slower field is in the opposite direction to the rear

magnet, produced much better results.

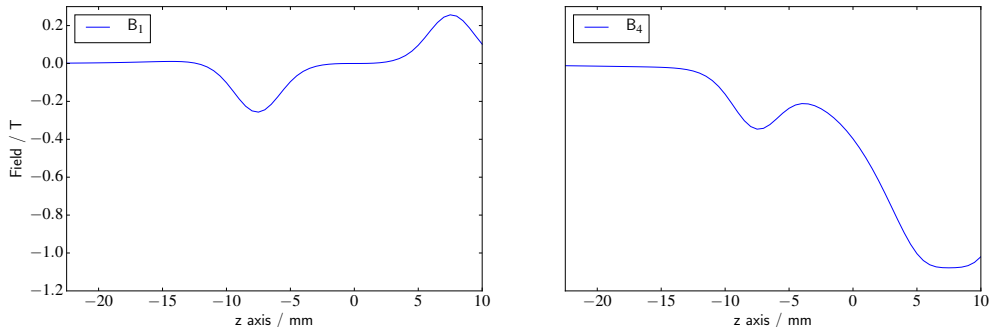


Figure 5.4: Trapping fields on z -axis. Left, trap only, right, slower coil at 460 A.

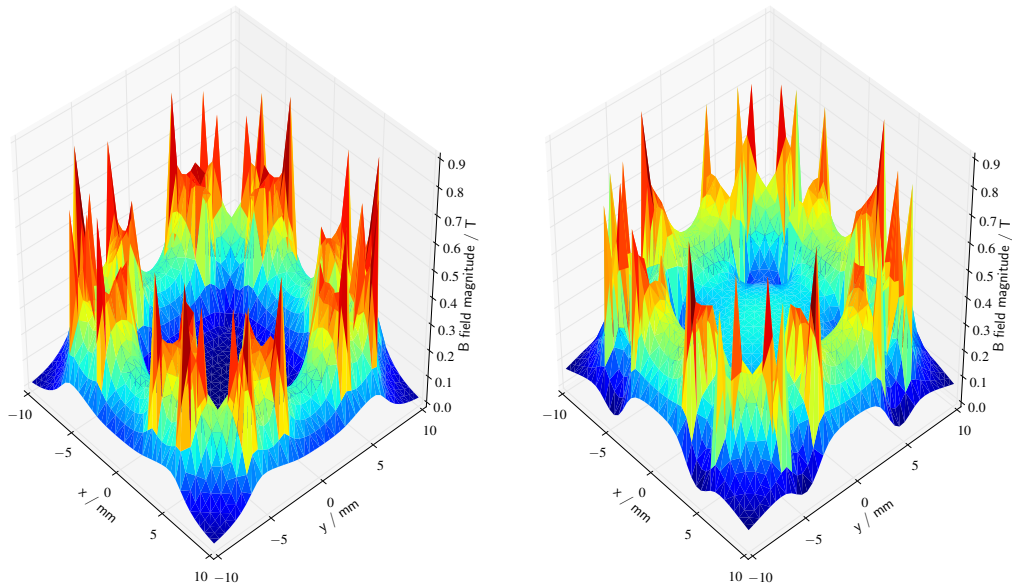


Figure 5.5: Trapping fields in xy -plane. Left, trap only, right, slower coil at 460 A.

The fields B_3 and B_4 for various values of the slower current were calculated, and used for Monte Carlo runs with the 3D simulator. As the coil switching times were based on the earlier 1D simulations [2] which had not included B_2 , it was also not included here. The switchover times are given in table 5.1.

Table 5.1: Switching times.

| Field | B_1 | B_3 | B_4 | B_1 |
|-----------|-------|--------|--------|--------|
| Time / ms | 0 | 0.5146 | 1.4181 | 2.3566 |

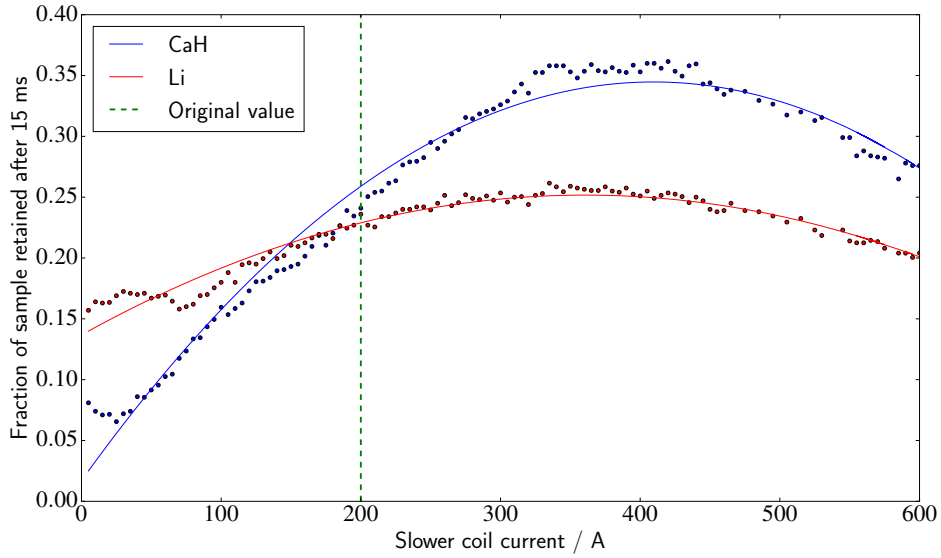


Figure 5.6: CaH and Li retention dependence on slower coil current.

Figure 5.6 shows how the percentage of the initial distribution of the two species retained varies with the current settings. Retention in the region of 35 % for CaH molecules and 25 % for Li atoms seemed feasible but we were aiming to achieve 50 % for CaH. Further optimisation work is discussed in the following section.

5.4 Trap loading - coil switching times

Choosing 400 A as being approximately optimal for the slower coil (see figure 5.6) we defined parameters $a - d$ as the times at which the different fields are switched in, see table 5.2. This now includes B_2 , as defined in table 3.1.

Table 5.2: Parameters representing the time at which a field is applied.

| Parameter | a | b | c | d |
|--------------------|-------|-------|-------|-------|
| Field switching in | B_2 | B_3 | B_4 | B_1 |

Figure 5.7 shows the results of a series of quick simulations varying the value of d . It can be seen that an immediate gain of over 10% CaH was achieved by shutting the slower off sooner.

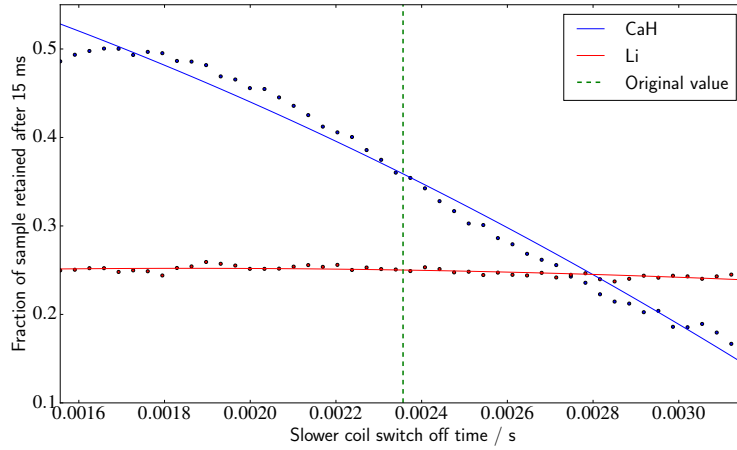


Figure 5.7: CaH and Li retention dependence on slower coil switch off time.

Further preliminary runs repeated this method for the other parameters, in an attempt to establish approximate ranges of valid values. Table 5.3 shows the results.

Table 5.3: Switching times - a set of values from each range were defined for each parameter.

| Parameter | Field active | Test range start / ms | Test range end / ms |
|-----------|--------------|-----------------------|---------------------|
| a | B_2 | 0.48 | 0.52 |
| b | B_3 | 0.78 | 0.82 |
| c | B_4 | 1.38 | 1.72 |
| d | B_1 | 1.40 | 1.72 |

Dividing each range into a number n of equally spaced values means n^4 combinations to test. It was also clear that the parameters would have different optimal values for different values of the slower current - for m different current settings we would therefore have a parameter space of mn^4 combinations to check - and this is neglecting repeat runs with different randomised initial distributions.

This all required thousands of simulation cycles. Low sample sizes were used with the Verlet algorithm, run in batches in parallel on the supercomputer. Each process was set to terminate on the retention count dropping below a set threshold. The overlap between c and d showed that the field B_4 is not needed for efficient loading.

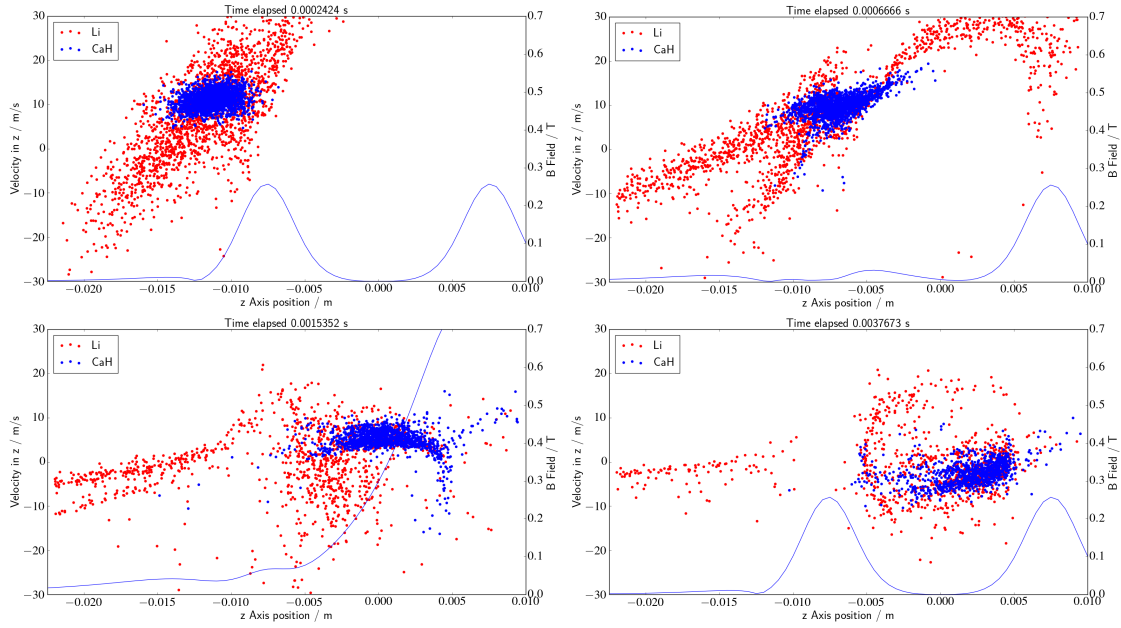


Figure 5.8: ‘Snapshots’ of 1D phase-space distribution on z -axis during co-loading CaH and Li into trap. On-axis field magnitude superimposed for reference.

Figure 5.8 shows plots of the phase-space distribution in z of the co-loaded species, with the magnitude of the on-axis B field superimposed for reference. In practice looking at these plots is of little help in optimising the switching times, as the full three-dimensional shape of the potential cannot be seen. Choosing parameter values by eye was generally unsuccessful - running a series of Monte-Carlo tests and looking at the results was a much more productive approach. Table 5.4 shows the values obtained. Overall a consistent retention of 56% CaH and 22% Li were achieved over 15 ms.

Table 5.4: Switching times - optimised at 460 A slower current.

| Parameter | a | b | c | d |
|-----------|------|------|-----|------|
| Time / ms | 0.52 | 0.78 | n/a | 1.68 |

5.5 Trap acceptance

The acceptance of the trap is defined as the portion of phase-space occupied by particles that can be successfully trapped. This was estimated by running Monte Carlo simulations of samples with random spatial coordinates and velocities, and allowing them to evolve for a period of time. Each point on the phase-space plots in figure 5.9 represents the initial co-ordinate of a particle that remained in the trap for 100 ms. The acceptance is roughly the same for each of the three axes shown; 122 mm m s^{-1} for CaH molecules and 300 mm m s^{-1} for Li atoms, estimated from the area of the plots.

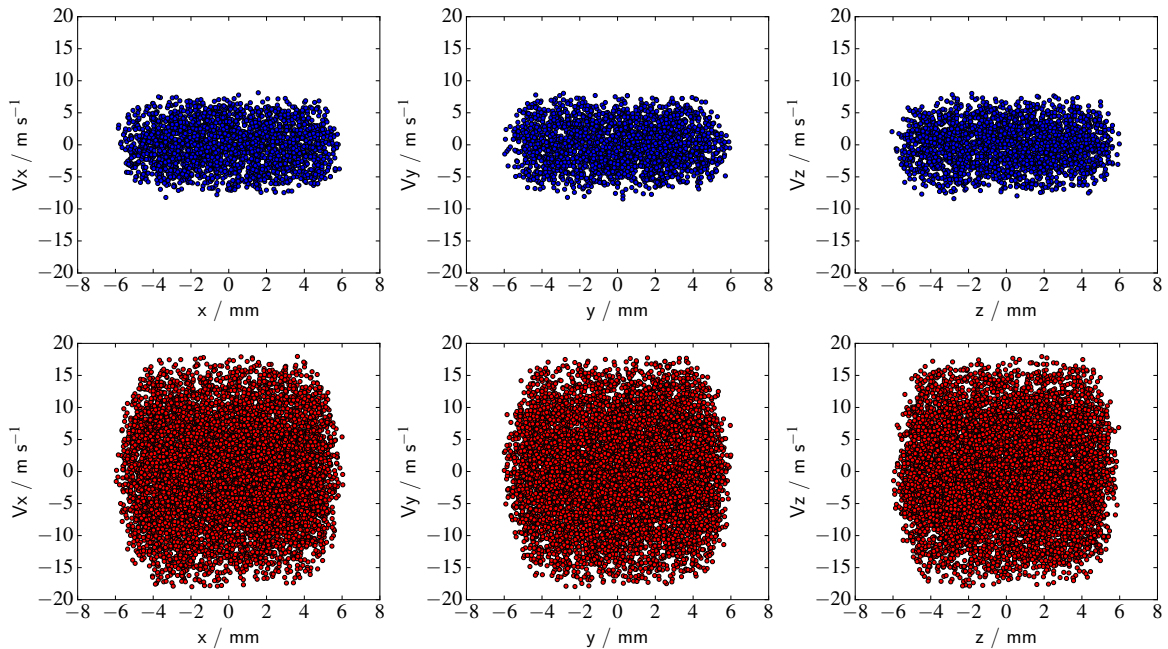


Figure 5.9: Initial phase-space distribution of particles that remain in trap over 100ms. Top, CaH, bottom, Li.

As discussed in section 3.2, the trap depth $|\mathbf{B}| \approx 0.113 \text{ T}$ (see figures 3.3 and 3.4). The Zeeman energy as a function of the magnitude of the magnetic field is $\Delta E = g_J \mu_B m_j B$; equating this to kinetic energy gives a maximum trapped speed for CaH of 5.54 m s^{-1} and for Li of 13.5 m s^{-1} , in reasonable agreement with figure 5.9.

5.6 Trap losses

Figure 5.10 shows the count of CaH molecules and Li atoms within 7.5 mm of the centre of the trap over 15 ms. The distance 7.5 mm was chosen to compare different loading parameters as it corresponds to the maximum trap depth. As the gas packets move into the centre of the trap there is an early peak, particularly for CaH, followed by a steady decline. The first part of this plot represents particles that are not loaded successfully; after the first few milliseconds the decay represents particles that escape after the trap is closed.

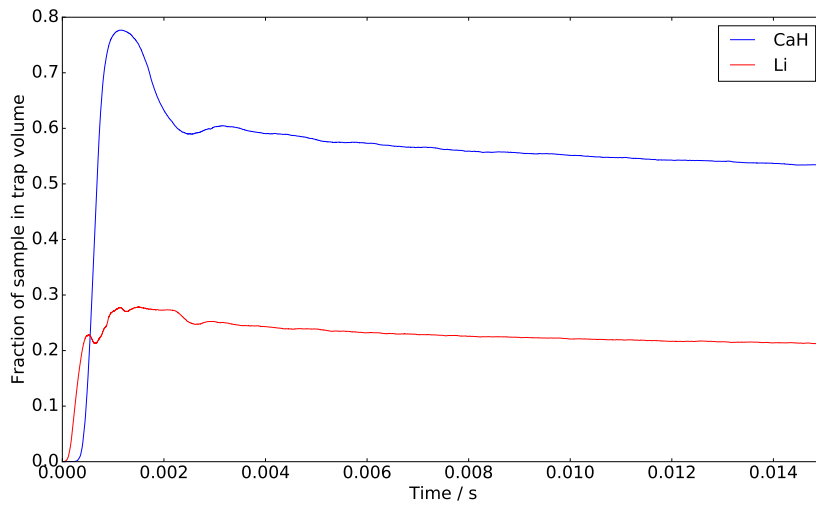


Figure 5.10: Sample within 7.5 mm of trap centre, optimised loading parameters as given earlier.

Table 5.5: Trap loss directions over 20 ms.

| Species | xy loss | negative z loss | positive z loss | remaining ($r \leq 7.5\text{mm}$) |
|---------|---------|-----------------|-----------------|-------------------------------------|
| CaH | 33 % | <1 % | 5 % | 56 % |
| Li | 33 % | 28 % | 16 % | 22 % |

Table 5.5 shows the results of logging the directions in which the particles leave the trap volume. The simulations show that Li has much higher losses in the z -direction than CaH - the internal temperature of the Li is higher, giving a broader range of velocities in z . Further changes to the loading sequence may help here. This is complicated by the fact that having the slowing and cancellation coils active can make portions of the trapping field defocusing, which plays a part in the significant losses in the xy -plane. Future work will model this part of the loading process more closely.

To investigate the losses occurring after the trap has closed, the simulations were adjusted to track full trajectories of particles escaping the interpolation area. Two examples are shown below:

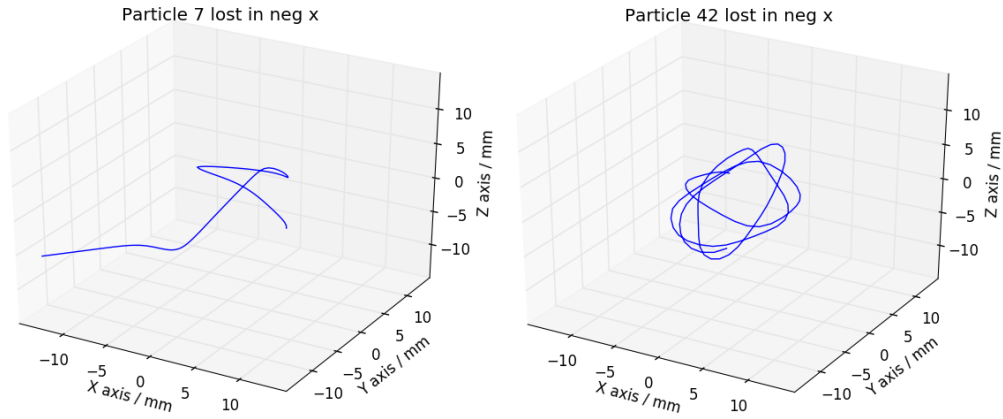


Figure 5.11: Example loss trajectories.

Extending these simulations to run up to 40 ms and plotting the results on top of each other is shown in figure 5.12.

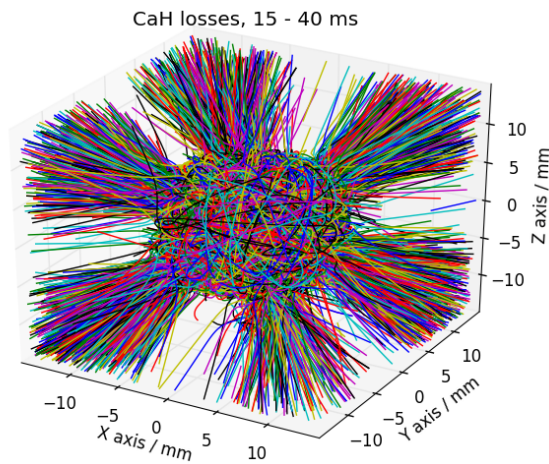


Figure 5.12: Each line in this plot is a trajectory that ultimately left the trap volume.

As discussed in section 3.2 the trap depth is not uniform, and the shallower parts of the potential lie around the diagonals. This can be seen in figure 5.12. Particles may spend some time orbiting in the centre of the trap before escaping.

5.7 Majorana losses

The adiabatic theorem in quantum mechanics as originally formulated by Born and Fock [58] states that if a perturbation on a system acts slowly enough the system remains in its instantaneous eigenstate. Particles trapped in a low-field seeking state can undergo Majorana transitions [59] ('spin-flips') to high-field seeking states and be ejected from a trap if they are unable to adiabatically follow changes in the magnetic field. Separating the centre-of-mass coordinates of the particle from the internal coordinates (as per the Born-Oppenheimer approximation) adiabatic energy states are defined [60] at these centre-of-mass coordinates \mathbf{r} , with eigenstates $|\phi_k\rangle$ and eigenenergies E_k :

$$H(\mathbf{r}) |\phi_k(\mathbf{r})\rangle = E_k(\mathbf{r}) |\phi_k(\mathbf{r})\rangle \quad (5.7.1)$$

The probability of transition from low-field-seeking, trapped states $|\phi_t\rangle$ to high-field-seeking untrapped states $|\phi_u\rangle$ has a maximum of [61]:

$$P_{max} \leq \left[\frac{\langle \phi_t | d/dt | \phi_u \rangle}{|E_t - E_u|/\hbar} \right]^2, \quad (5.7.2)$$

Therefore, the condition for adiabaticity can be written as:

$$|\langle \phi_t | \frac{d}{dt} | \phi_u \rangle| \ll \frac{|E_t - E_u|}{\hbar}. \quad (5.7.3)$$

Metcalf and van der Straten [10] give the adiabatic condition as $\omega_T \ll \omega_Z$, where ω_Z is the rate of Larmor precession and ω_T is the rate of change of orientation of the field, B - this is equivalent to inequality 5.7.3. Their work is in the context of the xy -plane in a quadrupole trap, in which the B field is zero at the centre and has a uniform gradient ∇B , so a circular path of radius ρ in the field will have a constant magnitude $\rho \nabla B$. For these classical circular orbits the rate of change of orientation of the field seen by the particles is their angular frequency $\omega_T = v/\rho$, which can be written:

$$\omega_T = \frac{1}{B} \frac{dB}{dt}. \quad (5.7.4)$$

The Larmor rate $\omega_Z = \mu_B B/\hbar$ so the adiabatic condition becomes:

$$\frac{1}{B} \frac{dB}{dt} \ll \frac{\mu_B B}{\hbar}, \quad (5.7.5)$$

and they also note that similar criteria will apply to more general orbits. Inequality 5.7.5 was used in simulations of a six-magnet trap by Nohlman [42] (via the relation $dB/dt = \nabla B \cdot v$) for Li at 4K. It was recognised that this only represented a worst-case scenario and that in actuality a range of non-unity probabilities for a transition exist, but the conclusion was that 80% of the atoms would be lost after 100 ms.

To determine whether this would be a useful test for our proposed trap the field magnitudes along circular paths of different radii in the axial planes as well as off-axis planes were calculated; some indicative results are shown in figure 5.13. In general there are no areas in the six-magnet trap where inequality 5.7.5 is valid.

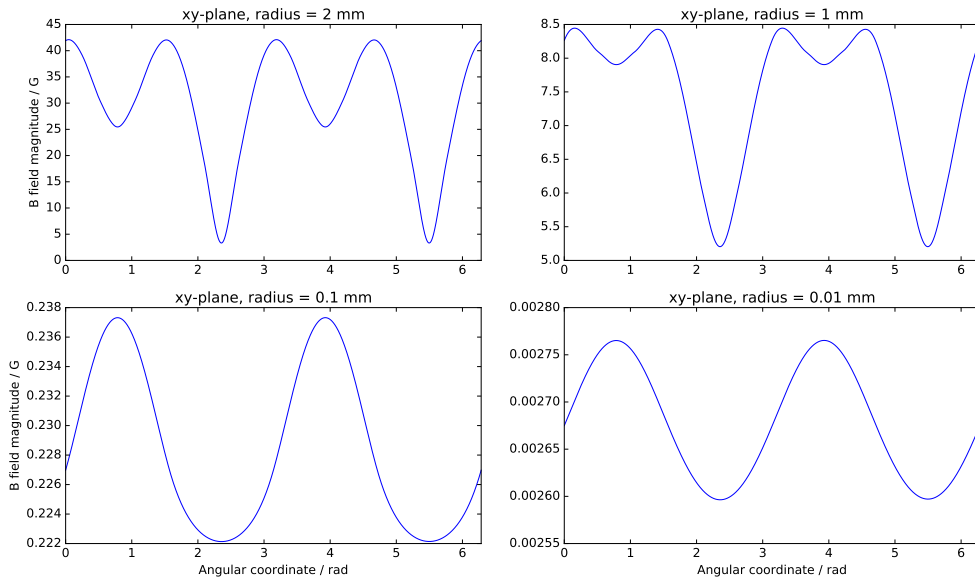


Figure 5.13: B field magnitude around circular paths, centred on the origin, in the xy -plane of the six-magnet trap. In order for inequality 5.7.5 to be applicable, each of these plots should have a constant magnitude $\rho \nabla B$.

Simulations were performed in order to make an estimate of the rate of loss from non-adiabatic transitions in our proposed trap. The direction of B at the location of each particle was found at time t and $t + h$; the angle between these vectors over this timestep gives a measure of ω_T . The magnitude of B at each point at t and $t + h$ was averaged to estimate ω_Z . If the ratio ω_Z/ω_T was not large enough, the particle was deemed to have been lost, and was removed from the sample. This is repeated at every iteration of the simulation.

The condition for adiabatic following is that the Larmor frequency is much larger than

the angular frequency with respect to the field orientation, but how large is large enough? A range of values for the violation threshold were tested, initially over a simulated trap time of 15 ms (to compare with earlier simulations).

Table 5.6: Estimated percentage loss to Majorana transition over 15 ms.

| Minimum ω_Z/ω_T | 10^0 | 10^1 | 10^2 | 10^3 | 10^4 | 10^5 |
|-----------------------------|--------|--------|--------|--------|--------|--------|
| CaH percentage loss | < 1 | < 1 | 3 | 19 | 46 | 67 |
| Li percentage loss | < 1 | < 1 | 4 | 20 | 32 | 39 |

Further runs extended the trap time to 100 ms:

Table 5.7: Estimated percentage loss to Majorana transition over 100 ms.

| Minimum ω_Z/ω_T | 10^0 | 10^1 | 10^2 | 10^3 | 10^4 | 10^5 |
|-----------------------------|--------|--------|--------|--------|--------|--------|
| CaH percentage loss | 1 | 2 | 13 | 46 | 59 | 67 |
| Li percentage loss | 1 | 3 | 13 | 26 | 32 | 39 |

In this admittedly limited study it can be seen that although the choice of violation threshold has a significant effect on the expected sample loss, the situation does not appear to be as dire as may have been feared. A more detailed study of the actual probabilities involved is under consideration for future work.

One possibility for ameliorating the effects of non-adiabatic transitions is the time-orbiting potential (TOP) trap [62, 36]. Here a uniform bias field is applied across the trap to shift the zero point, with the direction of the bias field rotating. The frequency of this rotation ω_b has to be much smaller than the Larmor frequency ω_Z so that the particles can adiabatically follow it, but larger than the particle oscillation in the static potential field, ω_T , in order to achieve a time-averaged potential [62]:

$$\omega_T \ll \omega_b \ll \omega_Z. \quad (5.7.6)$$

Future work will design and simulate a TOP mechanism to explore its applicability here.

5.8 Trap cooling - atomic density

The density and temperature of the sample of Li atoms after it has been laser cooled are important consideration for sympathetic cooling. As a preliminary assessment we simulated a uniform, spherical cloud of atoms in the centre of the trap, assumed to be instantaneously ‘cooled’ and then released to disperse. The fraction of the initial sample remaining in the approximate laser interaction volume (radius 1.5 mm) is shown in figure 5.14. The sample set to 1 mK had a density of approximately 50% after 20 ms, with a fitted temperature of 0.7 mK. The 5 mK result was 25% original density at about 3 mK. The remainder of the sample either moved to a stable trajectory further from the centre of the trap or was lost.

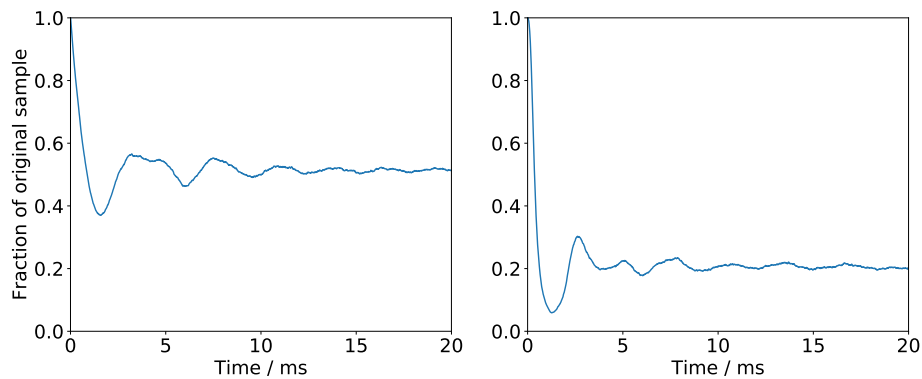


Figure 5.14: Cooled Li remaining in 1.5 mm radius; left, 1 mK, right, 5 mK.

In order to retain a significant fraction of the original density low Li temperatures need to be achieved. Alternatively, cooling lasers of larger radius could be used. The simulations were repeated for a beam radius of 2.8 mm; the corresponding results are shown in figure 5.15.

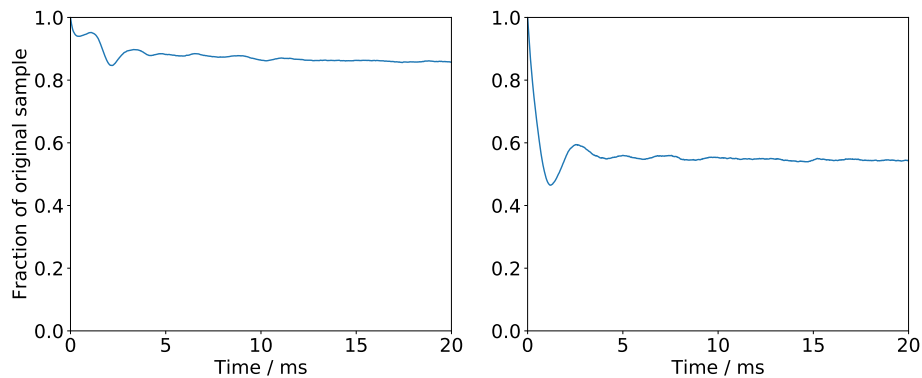


Figure 5.15: Cooled Li remaining in 2.8 mm radius; left, 1 mK, right, 5 mK.

The oscillations visible in figures 5.14 and 5.15 can be explained as follows: in the first 2 ms, the higher-energy portion of the sample located in the trap centre expands, causing a rapid drop in density. The lower-energy parts of the sample located further out in the trap migrate inwards by about 3 ms, increasing the density again. Meanwhile, the high-energy particles from all across the simulated cloud ricochet around the trap, often crossing the ‘detection’ volume, until they find the weakest parts of the field and escape. By approximately 11 ms most of the non-phase-stable particles are lost; due to the non-uniform trapping potential across the surface of the detection volume there are still some small oscillations.

5.9 Trap cooling - laser interaction

Simulations were designed to determine the time evolution of the fraction of the Li sample entering the laser-cooling region at least once. As a first approximation the volume where the lasers intersect was simply defined as a sphere of radius 1.5 mm at the centre of the trap. Monte Carlo distributions of Li at the point when the trap has just closed (based on the results of the earlier sample loading work) were then allowed to evolve under the confinement of the permanent magnets only, and the atoms were flagged when they entered the central region. This was repeated for the 2.8 mm radius beam considered in the last section, and figure 5.16 shows the averaged results over 20 ms. (Atoms are not counted twice).

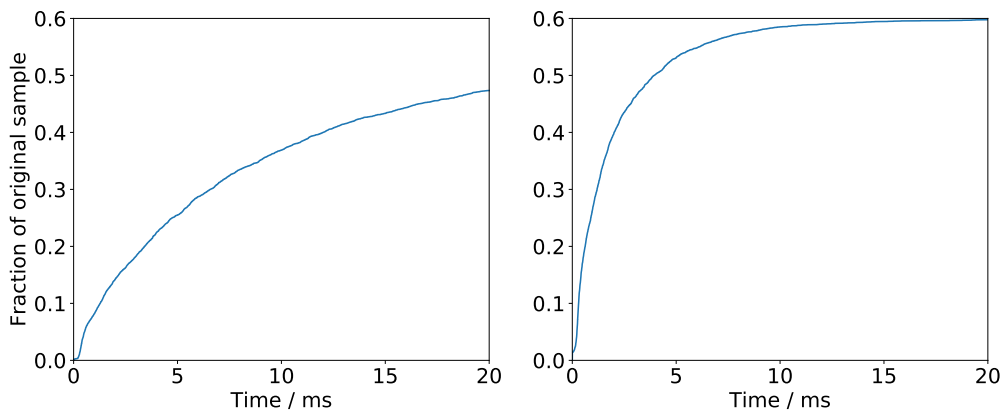


Figure 5.16: Fraction of Li sample entering the intersection of the cooling lasers at least once over 20 ms; left, 1.5 mm radius, right, 2.8 mm radius.

This work did not attempt to model the interaction of the Li atoms with the cooling lasers, and also did not account for the intensity profile of a real laser, or the actual shape of the beam intersections.

Chapter 6

Conclusions

6.1 Review

We have proposed a hybrid trap based on six toroidal magnets with two solenoid-type coils to operate with our existing moving-trap Zeeman Decelerator experiment. This trap is intended to receive co-decelerated atomic and molecular species, and cool them via a combination of laser and sympathetic cooling. Applications are primarily intended to be the study of ultra-cold chemical reactions.

A detailed review of our simulation methodology has been given, including a software interpolator, and different numerical integration methods, with a consideration of the likely errors arising from these methods.

The proposed trap has been tested with simulations of lithium and calcium hydride, based on previous Zeeman deceleration simulations of these species. We have determined indicative operating parameters for the trap to achieve reasonable capture efficiencies. Studies of potential loss mechanisms and ways to alleviate these effects have been undertaken.

A recap of the proposed procedure (for a basic sympathetic cooling experiment) is:

- Co-decelerated CaH molecules and Li atoms delivered from moving-trap Zeeman decelerator
- Cancellation coil ‘opens’ magnetic trap / magneto-optical trap, slower coil provides final deceleration
- Coils off, sample loaded into trap, cooling lasers on to extract energy from Li
- Lasers off, time-orbiting-potential coils on to suppress Majorana losses, CaH cooled by elastic collisions with Li

6.2 Outlook

There are several areas suggested for the extension of the work covered in this report. Firstly, the trap-loading simulations feature hard switchovers between the different field regimes, whereas in reality any power supply capable of supplying the cancellation and slower coils will have rise and fall times that are significant on the timescale of the trap loading process. The Zeeman decelerator built by our group has a wire quadrupole which carries a current on the order of hundreds of amps over several milliseconds, which is similar to the requirements of the trap, and has a rise time of several hundred microseconds. A ‘kick’ circuit has been designed and incorporated to reduce this rise time by over a factor of five, using capacitors (the associated fall time is likely to remain several times larger than this). Even assuming a rise time $t \approx 50 \mu\text{s}$, it would be desirable to incorporate the changing trap fields in simulations, as the typical time step we employ is $0.1 \mu\text{s}$. It is very likely that this would significantly alter the optimised trap parameters discussed here.

The longitudinal speed of the sample packet as it leaves the decelerator and is loaded into the trap was chosen herein to be 11.2 m s^{-1} . There is of course a compromise to be made here - faster packets have a shorter time of unconfined flight, but the trap then has to remove more kinetic energy to capture them. Some Monte Carlo simulations were done to look at varying the packet speed and should be revisited, although more promising is the concept of pulsing the cancellation coil on more than once, to engage the CaH and Li separately. This will depend on the current rise times for its feasibility.

So far, the only work done on the laser-cooling aspect of the trap is the estimation of the timescale over which the Li atoms will sample the volume at the intersection of the lasers. It would be desirable to model the laser interaction and beam profiles more accurately. The evolution of atomic samples with different representative temperatures was tentatively explored but more detailed simulations will cover the actual phase-space compression process. Another group in Durham has performed detailed simulations of a magneto-optical trap [63], and we intend to apply their methods to our experiment. We have demonstrated that cooling beams of larger radius may be desirable, which would require some adjustment to our preliminary trap design as described. Work described in this report can be easily extended to compare different magnet properties.

Some consideration has been given here to Majorana spin-flip transitions, and the resulting losses to high-field-seeking states. We have extended a method given in [42] to cover general orbits in a spatially varying magnetic field rather than the limited case of circular orbits in the centre of a quadrupole field, at least in as far as producing an inequality that represents a worst-case scenario for particle loss. It would be instructive to try and more accurately represent the rate of Majorana loss, potentially by calculating the quantum mechanical probabilities for each particle at each time step, and we have had preliminary discussions with theoretician colleagues regarding this. We have already started working on TOP trap designs.

Bibliography

- [1] Mizouri, A. (2016), ‘*A Moving-Trap Zeeman Decelerator*’, PhD thesis, Durham University.
- [2] McArd, L. M. (2017), ‘*A Travelling Wave Zeeman Decelerator For Atoms and Molecules*’, PhD thesis, Durham University.
- [3] Feynman, R. (1982). ‘Simulating Physics with Computers’, *International Journal of Theoretical Physics*, Vol. 21, pp. 467488. DOI:10.1007/BF02650179
- [4] Orzel, C. (2017) *Quantum Simulation*, IOP Publishing . DOI: 10.1088/978-0-7503-1516-6
- [5] Ospelkaus, S. *et al.*, (2010) ‘Quantum-state controlled chemical reactions of ultracold potassium-rubidium molecules’, *Science* Vol. 327, pp. 853857 DOI:10.1126/science.1184121
- [6] Skouteris, D. (1999) *et al.*, ‘van der Waals Interactions in the Cl + HD Reaction’, *Science*, Vol. 286, pp 1713-1716, DOI:10.1126/science.286.5445.1713
- [7] Knoop, S. *et al.*, (2010) ‘Magnetically Controlled Exchange Process in an Ultracold Atom-Dimer Mixture’, *Phys. Rev. Lett.*, Vol. 104, p. 053201, DOI:10.1103/PhysRevLett.104.053201
- [8] Köhler, Thorsten and Góral, Krzysztof and Julienne, Paul S. (2006) ‘Production of cold molecules via magnetically tunable Feshbach resonances’, *Rev. Mod. Phys.*, Vol. 78, pp. 1311–1361, DOI:10.1103/RevModPhys.78.1311
- [9] Phillips, W. D. and Metcalf, H. (1982) ‘Laser Deceleration of an Atomic Beam’, *Phys. Rev. Lett.*, Vol. 48, pp. 596-599, DOI:10.1103/PhysRevLett.48.596
- [10] Metcalf, H. and van der Straten, P. (1999) *Laser Cooling and Trapping*, New York, Springer-Verlag.
- [11] Zhelyazkova, V. and Cournol, A. and Wall, T. E. and Matsushima, A. and Hudson, J. J. and Hinds, E. A. and Tarbutt, M. R. and Sauer, B. E. (2014) ‘Laser cooling and slowing of CaF molecules’, *Phys. Rev. A*, Vol. 89, pp. 053416–21, DOI:10.1103/PhysRevA.89.053416

- [12] Barry, J. F. and McCarron, D. J. and Norrgard, E. B. and Steinecker, M. H. and DeMille, D., (2014) 'Magneto-optical trapping of a diatomic molecule', *Nature*, Vol. 512, p. 286, DOI:10.1038/nature13634
- [13] Hogan, Stephen D. and Motsch, Michael and Merkt, Frdric (2011) 'Deceleration of supersonic beams using inhomogeneous electric and magnetic fields', *Phys. Chem. Chem. Phys.*, Vol. 13, pp. 18705–18723, DOI:10.1039/C1CP21733J
- [14] Vanhaecke, N., Meier, U., Andrist, M., Meier, B. and Merkt, F. (2007) 'Multi-stage Zeeman deceleration of hydrogen atoms', *Phys. Rev. A*, Vol. 75, pp. 031402-6, DOI:10.1103/PhysRevA.75.031402
- [15] Narevicius, Edvardas and Libson, Adam and Parthey, Christian G. and Chavez, Isaac and Narevicius, Julia and Even, Uzi and Raizen, Mark G., (2008) 'Stopping Supersonic Beams with a Series of Pulsed Electromagnetic Coils: An Atomic Coilgun', *Phys. Rev. Lett.*, Vol. 100, pp. 093003–6, DOI:10.1103/PhysRevLett.100.093003f
- [16] Akerman, N. *et al.* (2017) 'Trapping of Molecular Oxygen together with Lithium Atoms', *Phys. Rev. Lett.*, Vol. 119, pp. 073204-9, DOI:10.1103/PhysRevLett.119.073204
- [17] Truppe, S. (2017) 'A buffer gas beam source for short, intense and slow molecular pulses', *arXiv*, arXiv:1707.06291
- [18] Singh, V. *et al.*, (2012) 'Chemical Reactions of Atomic Lithium and Molecular Calcium Monohydride at 1 K', *Physical Review Letters*, DOI:10.1103/PhysRevLett.108.203201
- [19] Foot, C. J. (2004) *Atomic Physics*, Oxford, Oxford University Press
- [20] Boland, B. J., Brown, J. M., Carrington, A. and Nelson A. C. (1978) 'Microwave Spectroscopy of Nonlinear Free Radicals. III. High Field Zeeman Effect in HCO and DCO', *Proceedings of the Royal Society of London. Series A, Mathematical and Physical Sciences*, Vol. 360, pp. 507-528, <https://www.jstor.org/stable/79546>
- [21] Berg, L.E. and Klynning, L. (1974) 'Rotational Analysis of the A-X and B-X Band Systems of CaH', *Physica Scripta*, Vol. 10, pp. 331, <http://iopscience.iop.org/article/10.1088/0031-8949/10/6/009/meta>
- [22] Einstein, A. (1917) 'Zur Quantentheorie der Strahlung', *Zeitschrift für Physik*, Vol. 18, No. 121

- [23] Compton, A. H., (1923), 'The Spectrum of Scattered X-Rays', *Phys. Rev.*, Vol. 22, pp. 409-413, DOI:10.1103/PhysRev.22.409
- [24] Frisch, R. (1933) 'Experimenteller Nachweis des Einsteinschen Strahlungsrückstoßes', *Zeitschrift für Physik*, Vol. 86, pp. 42-48
- [25] Ashkin, A., Dziedzic, J.M., Bjorkholm, J.E. and Chu, S. (1986) 'Observation of a single-beam gradient force optical trap for dielectric particles', *Opt. Lett.*, Vol. 11, pp. 288-290, DOI:10.1364/OL.11.000288
- [26] Wineland, D. J. and Dehmelt, H. (1975) 'Proposed $10^{14} \delta\nu/\nu$ laser fluorescence spectroscopy on Tl^+ mono-ion oscillator III (side band cooling)', *Bull. Am. Phys. Soc.*, Vol. 20, No. 637
- [27] Hänsch, T. W. and Schawlow, A. L. (1975) 'Cooling of gases by laser radiation', *Opt. Commun.* Vol. 13, No. 68
- [28] Gerlach, W. and Stern O. (1922) 'Der experimentelle Nachweis des magnetischen Moments des Silberatoms', 'Zeitschrift für Physik', Vol. 8, p. 110.
- [29] Friedburg, H. and Paul W. (1951) 'Optische Abbildung mit neutralen Atomen', *Naturwissenschaften*, Vol. 38 p. 159.
- [30] Even, U. (2015) 'The Even-Lavie valve as a source for high intensity supersonic beam', *EPJ Techniques and Instrumentation*, Vol. 2, p. 17, DOI:10.1140/epjti/s40485-015-0027-5
- [31] Campargue, R. (2001) *Atomic and Molecular Beams*, Berlin, Springer-Verlag
- [32] Trimeche, A., Bera, M. N., Cromières, J. -P., Robert, J. and Vanhaecke, N. (2011) 'Trapping of a supersonic beam in a traveling magnetic wave', *The European Physical Journal D*, Vol. 65, pp. 263-271
- [33] 'Liouville's theorem', *Wikipedia*. Available at: [https://en.wikipedia.org/wiki/Liouville's_theorem_\(Hamiltonian\)](https://en.wikipedia.org/wiki/Liouville's_theorem_(Hamiltonian))
- [34] Raab, E. L., Prentiss, M., Cable, A., Chu, S. and Pritchard, D. E. (1987) 'Trapping of Neutral Sodium Atoms with Radiation Pressure', *Phys. Rev. Lett.*, Vol. 59, pp. 2631-2634, DOI:10.1103/PhysRevLett.59.2631
- [35] Hess, H., (1986) 'Evaporative cooling of magnetically trapped and compressed spin-polarized hydrogen', *Phys. Rev. B*, Vol. 34, No. 5, pp. 3476-3479, DOI:10.1103/PhysRevB.34.3476

- [36] Petrich, W., Anderson, M., Ensher, J. and Cornell, E. (1995) ‘Stable, Tightly Confining Magnetic Trap for Evaporative Cooling of Neutral Atoms’, *Phys. Rev. Lett.*, Vol. 74, pp. 3352 - 3355 . DOI:10.1103/PhysRevLett.74.3352
- [37] Anderson, M. H., Ensher, J.R., Matthews, M.R., Wieman, C.E. and Cornell, E.A. (1995) ‘Observation of Bose-Einstein Condensation in a Dilute Atomic Vapor’, *Science*, Vol. 269, pp. 198-201, DOI:10.1126/science.269.5221.198
- [38] Myatt, C. J., Burt, E. A., Ghrist, R. W., Cornell, E. A., and Wieman, C. E. (1997) ‘Production of Two Overlapping Bose-Einstein Condensates by Sympathetic Cooling’, *Phys. Rev. Lett.*, Vol. 78, pp. 586-589, DOI:10.1103/PhysRevLett.78.586
- [39] Guggemos, M., Heinrich, D., Herrera-Sancho, O., Blatt, R. and Roos, C. (2015) ‘Sympathetic cooling and detection of a hot trapped ion by a cold one’, *New Journal of Physics*, Vol. 17, pp. 103001, DOI:10.1088/1367-2630/17/10/103001
- [40] Lim, J., Frye, M., Hutson, J. and Tarbutt, M. (2015) ‘Modeling sympathetic cooling of molecules by ultracold atoms’, *Phys. Rev. A*, Vol. 92, p. 053419, DOI:10.1103/PhysRevA.92.053419
- [41] Tokunaga, S.K., Skomorowski, W., Zuchowski, P.S. *et al.* (2011) ‘Prospects for sympathetic cooling of molecules in electrostatic, ac and microwave traps’, *Eur. Phys. J. D* Vol. 65, pp. 141-149, DOI:10.1140/epjd/e2011-10719-x
- [42] Nohlman, D. (2015) ‘*A Permanent Magnet Trap For Buffer Gas Cooled Atoms*’, PhD thesis, University College London, <https://goo.gl/ffAeeu> [Accessed June 2017].
- [43] Dubas, F. and Espanet, C. (2009) ‘Analytical Solution of the Magnetic Field in Permanent-Magnet Motors Taking Into Account Slotting Effect: No-Load Vector Potential and Flux Density Calculation’, *IEEE Transactions on Magnetics*, Vol. 45, pp. 2097-2109, DOI:10.1109/TMAG.2009.2013245
- [44] Meeker, D. (2013) ‘Improvised Open Boundary Conditions for Magnetic Finite Elements’, *IEEE Transactions on Magnetics*, Vol. 49, pp. 5243-5247, DOI:10.1109/TMAG.2013.2260348
- [45] ‘Radia Introduction’, (2017), *ESRF* . Available at: <http://www.esrf.eu/Accelerators/Groups/InsertionDevices/Software/Radia/Documentation/Introduction>

- [46] ‘Spline interpolation’, *Wikipedia*. Available at: https://en.wikipedia.org/wiki/Spline_interpolation
- [47] ‘Interpolation (scipy.interpolate) - SciPy v0.19.0 Reference Guide’, (2017), *SciPy.org* . Available at: <https://docs.scipy.org/doc/scipy/reference/interpolate.html>
- [48] Kadosh A., Cohen-Or D. and Yagel R. (2003) ‘Tricubic interpolation of discrete surfaces for binary volumes’, *IEEE Transactions on Visualization and Computer Graphics*, Vol. 9, No. 4, pp. 580 586 . DOI: 10.1109/TVCG.2003.1260750
- [49] Lekien, F. and Marsden, J. (2005) ‘Tricubic interpolation in three dimensions’, *International Journal for Numerical Methods in Engineering*, Vol. 63, No. 3, pp. 455471 . DOI: 10.1002/nme.1296
- [50] Iskandarani, M. ‘Finite Difference Approximation of Derivatives’, , Rosenstiel School of Marine and Atmospheric Science. Available at <https://www.rsmas.miami.edu/users/miskandarani/Courses/MSC321/lectfiniteDifference.pdf> [Accessed October 2017].
- [51] Press, W. Flannery, B., Teukolsky, S. and Vetterling, W. (2007), *Numerical Recipes: The Art of Scientific Computing (3rd ed.)*, Cambridge, Cambridge University Press.
- [52] Voesenek C.J. ‘OrbitRungeKutta4.pdf’, (2014) *Rochester Institute of Technology* . Available at <http://spiff.rit.edu/richmond/nbody/OrbitRungeKutta4.pdf> [Accessed April 2017].
- [53] Verlet, L. (1967) ‘Computer “Experiments” on Classical Fluids. I. Thermodynamical Properties of Lennard-Jones Molecules’, *Physical Review*, Vol. 159, No. 1, pp. 98103 . DOI:10.1103/PhysRev.159.98
- [54] Allen, M. P. and Tildesley, D. J. (2017) *Computer Simulation of Liquids, Second Edition*, Oxford, Oxford University Press.
- [55] Frenkel, D. and Smit, B. (1996) ‘*Understanding Molecular Simulation: From Algorithms to Applications*’, Orlando, Academic Press, Inc.
- [56] ‘Runge-Kutta methods’, (2017) *Wikipedia* . Available at: https://en.wikipedia.org/wiki/Runge-Kutta_methods [Accessed April 2017].
- [57] Fehlberg, E. (1970) ‘Klassische Runge-Kutta-Formeln vierter und niedrigerer Ordnung mit Schrittweiten-Kontrolle und ihre Anwendung auf Wrmeleitungsprobleme’, *Computing (Arch. Elektron. Rechnen)*, Vol. 6, pp. 6171, DOI:10.1007/BF02241732

- [58] Born, M. and Fock, V. (1928) ‘Beweis des Adiabatsatzes’, *Zeitschrift für Physik A.*, Vol. 51, pp. 165-180. DOI:10.1007/BF01343193.
- [59] Majorana, E. (1932) ‘Atomi orientati in campo magnetico variabile’, *Nuovo Cimento*, Vol. 9, pp. 4350.
- [60] Lara, M., Lev, B. and Bohn, J. (2008), ‘Loss of molecules in magneto-electrostatic traps due to nonadiabatic transitions’, *Phys. Rev. A*, Vol. 78, No. 3, pp. 033433-1 - 033433-11 . DOI: 10.1103/PhysRevA.78.033433
- [61] Messiah, A. (1961) *Quantum Mechanics*, New York, Dover Publications, Inc.
- [62] Minogin, V., Richmond, J. and Opat, G. (1998) ‘Time-orbiting-potential quadrupole magnetic trap for cold atoms’, *Phys. Rev. A*, Vol. 58, pp. 3138 - 3145, . DOI:10.1103/PhysRevA.58.3138
- [63] Hanley, R. K., Huillery, P., Keegan, N. C., Bounds, A. D., Boddy, D., Faoro, R., and Jones, M. P. A. (2018) ‘Quantitative simulation of a magneto- optical trap operating near the photon recoil limit’, *Journal of Modern Optics*, Vol. 65, pp. 667-676, DOI:10.1080/09500340.2017.1401679